Schweizerischer Erdbebendienst
Service Sismologique Suisse
Servizio Sismico Svizzero
Swiss Seismological Service

ETH zürich

SITE CHARACTERIZATION REPORT

SWIM: Wildhaus (SG) - Mehrzweckhalle

Manuel Hobiger, Donat Fäh

Last Modification: 27/05/2021

Schweizerischer Erdbebendienst (SED)
Service Sismologique Suisse
Servizio Sismico Svizzero
Servizi da Terratrembels Svizzer

ETH Zürich
Sonneggstrasse 5
8092 Zürich
Schweiz
manuel.hobiger@sed.ethz.ch

Contents

Summary

The free-field strong-motion station SWIM was built in Wildhaus-Alt St. Johann (SG) close to the Mehrzweckhalle. We performed a passive seismic array measurement with two array configurations to characterize the soil underneath the station.
The measurements show that the fundamental frequency of the structure beneath the station is about 5.63 Hz. Dispersion curves for Love and Rayleigh waves were retrieved between 3.5 and 37.1 Hz and 4.9 and 28.1 Hz, respectively, but the high-frequency parts of these curves are not representative for the permanent station.
Inversions using two different targets were performed, where the first is representative for station SWIM and does not contain the high-frequency dispersion curves and the second is representative for the parking lot nearby.
The inversion results indicate that the area around station SWIM is characterized by a shallow layer of 1 to 1.6 m depth with an S-wave velocity between 65 and 155 m/s, followed by a second layer with a velocity between 560 and 650 m/s down to about 10 m, where the seismic bedrock with a velocity of about 900 m/s is found. Below, the velocities gradually increase. The V_{S30} value is (673.6 ± 9.9) m/s. For the second inversion centered on the parking lot, it is (651.4 ± 2.9) m/s.
This corresponds to soil class B for both SIA261 and EC8 in both cases.

1 Introduction

In the framework of the second phase of the Swiss Strong Motion Network (SSMNet) renewal project, a new station was planned in Wildhaus-Alt St. Johann (SG). The Mehrzweckhalle was selected as installation site. The new station, called SWIM, went operational on 17 October 2019. The location of the station with respect to other SSMNet stations is shown in Fig. 1.

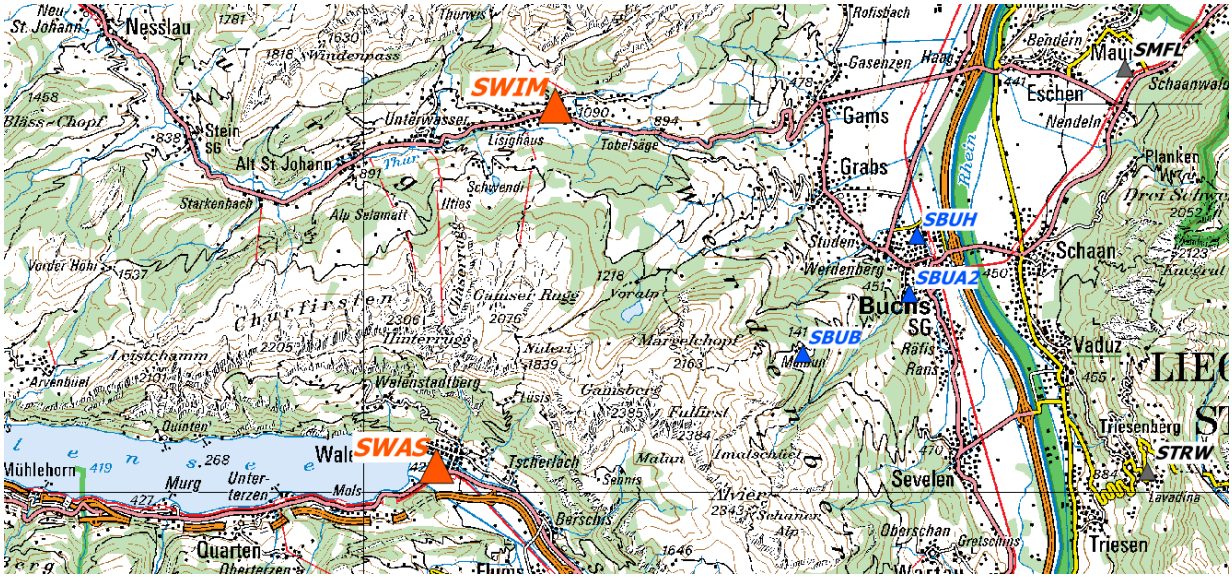

Figure 1: Map showing the location of station SWIM, together with other stations of the first phase of the SSMNet renewal project (blue triangles) and the second phase (orange triangles).

2 Geological setting

A geological map of the surroundings of station SWIM is shown in Fig. 2, with the sensor locations of the passive measurements as orientation. Station SWIM is located on moraine, as most stations of the passive seismic array. To the northwest, outcroppings of marl lime, marl, and micrite are found.

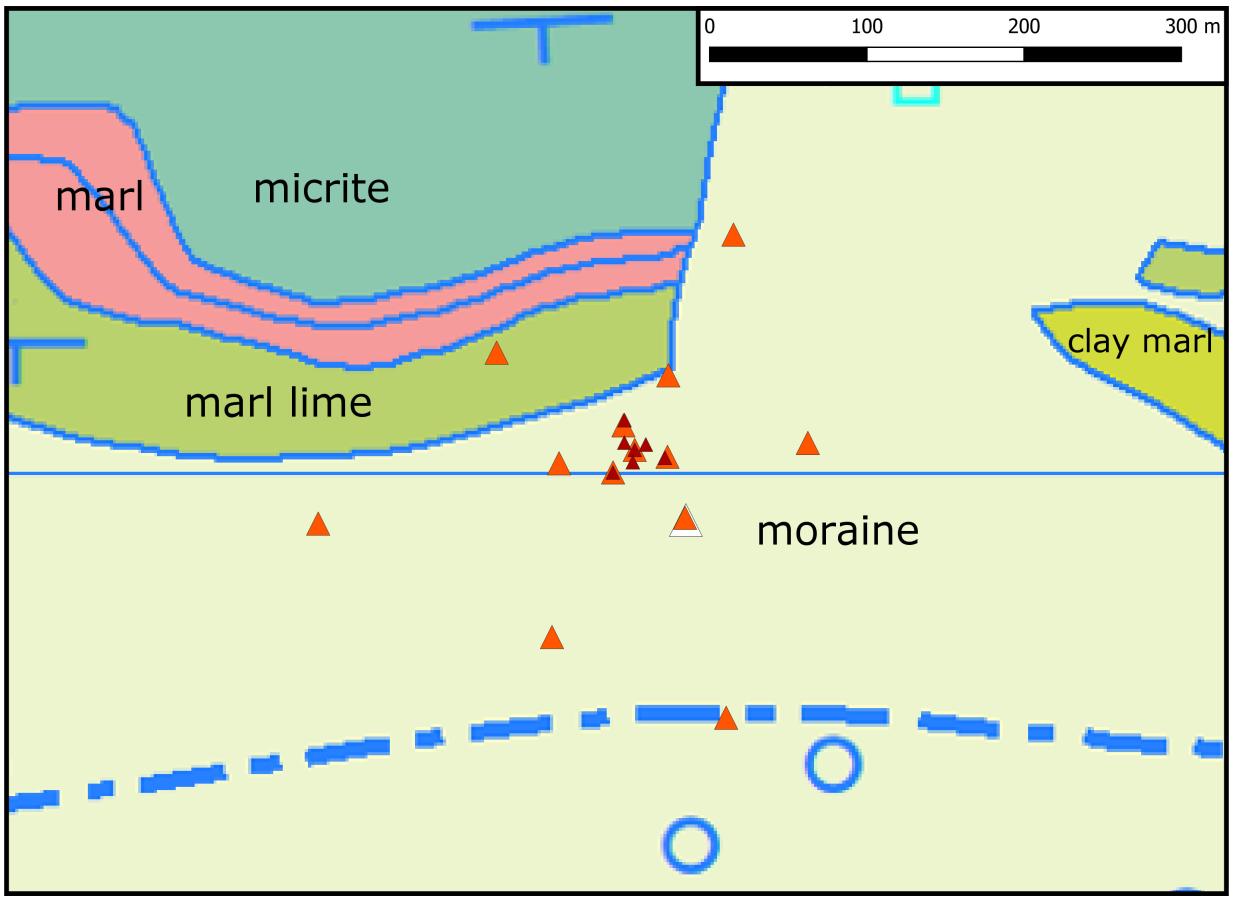

Figure 2: Geological map of the area around station SWIM, highlighting the location of the array stations (see next section). According to the geological atlas, station SWIM lies on moraine. Source: Federal Office of Topography.

3 Site characterization measurements

3.1 Data set

In order to characterize the local underground structure around station SWIM, a passive seismic array measurement was carried out on 19 August 2020. The layout of the seismic measurement is shown in Fig. 3.
Two array measurements were performed (see Table 1 for the main characteristics). The first array was planned to consist of 13 stations, distributed in four rings of three stations each and a central station, with ring radii of 20 m, 50 m, 120 m, and 250 m, respectively. The center of the array was located on a parking lot.
The second array consisted of the innermost ring of the first array, where the stations had been slightly shifted, and an additional inner ring with radius of around 8 m. This measurement was performed in the late afternoon, as the parking lot was less crowded at that time.
Only the central station and the inner ring of array 2 were also analyzed together, forming array 3.
The names of the stations of the first array are composed of "SWIM" followed by a two-digit number (42 to 49, 52 to 55, 73), indicating the serial number of the digitizers. Sensor SWIM73 was connected to the B channel of digitizer 53, all other sensors were connected to the respective A channels. The seismic stations consisted of Lennartz 3C 5 s sensors connected to Centaur digitizers. The station names in the second (and third) array are composed of "SWIM" and a two-digit number (83, 86, 87, 88, 92, 93, 99), corresponding to the serial number plus 40 for the first six. SWIM99 was connected to the B channel of digitizer 53.
The station locations have been measured by a differential GPS system (Leica Viva GS10) which was set up to measure with a precision better than 5 cm. This precision was achieved for all stations except SWIM54, the northernmost station of array 1, where the precision was only 1.39 m. This station is the outermost station of the array. The different stations also show differences in the elevation. The parking lot, where the inner array stations were installed, has an altitude between 1095 and 1098 m. The stations to the southeast have similar elevations. The three stations to the north and west of the parking lot are located on altitudes between 1112 and 1117 m. This topographic effect might have an influence on the array measurements at low frequencies.

Table 1: List of the passive seismic array measurements in Wildhaus. Array 3 is a sub-array of array 2.

Array name	Number of sensors	Minimum interstation distance [m]	Maximum interstation distance [m]	Recording time [s]
1	13	17.2	321.7	9240
2	7	7.8	35.2	3300
3	4	7.8	13.9	3300

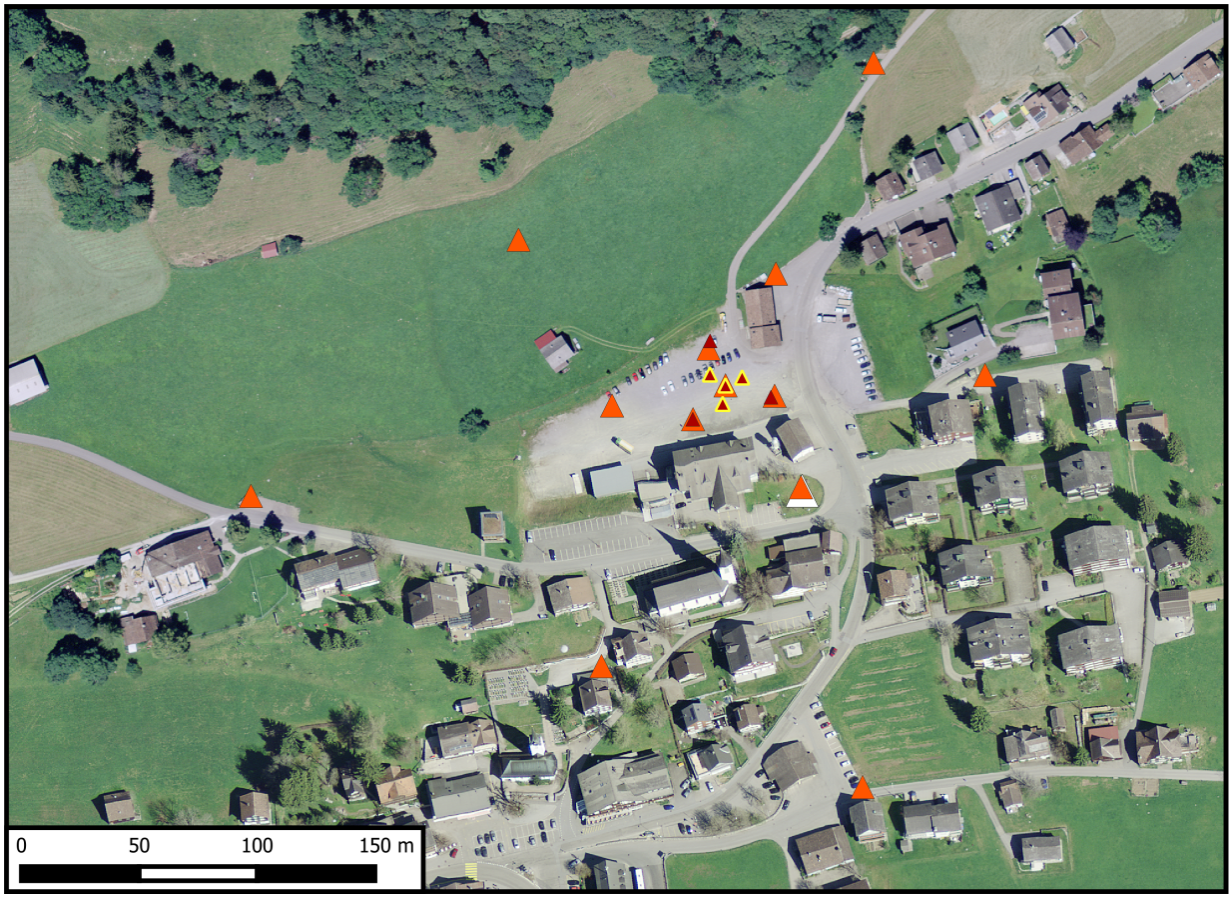

Figure 3: Layout of the array measurements around station SWIM. The location of SWIM is indicated by the white triangle, the locations of the stations for the passive seismic measurement by the orange triangles (first array) and red triangles (second array). The yellow triangles indicate the third array. Source: Federal Office of Topography.

3.2 H/V and RayDec ellipticity curves

Figure 4 shows the H/V curves determined with the time-frequency analysis method (Fäh et al., 2009) for all stations of both passive arrays. The curves are mostly flat at low frequencies and show a wide variability of the peak frequency for all stations, ranging from 3.7 to 18.8 Hz. Fig. 5 gives an overview of the peak frequencies for all stations. For some stations on the parking lot, no H/V peak was picked. The station next to SWIM has a peak frequency of 5.63 Hz. The stations on the parking lot for which a peak was picked have peak frequencies between 8 and 14 Hz. The stations where no peak was picked might actually have a peak above 20 Hz. This reflects the heterogeneity of the site. The peaks are probably linked with very shallow layers at the surface.
The RayDec technique (Hobiger et al., 2009) is supposed to eliminate the contributions of other wave types than Rayleigh waves and give a better estimate of the ellipticity than the classical H/V technique. The RayDec ellipticity curves for all stations of the array measurements are shown in Fig. 4 and are similar to the H/V curves.

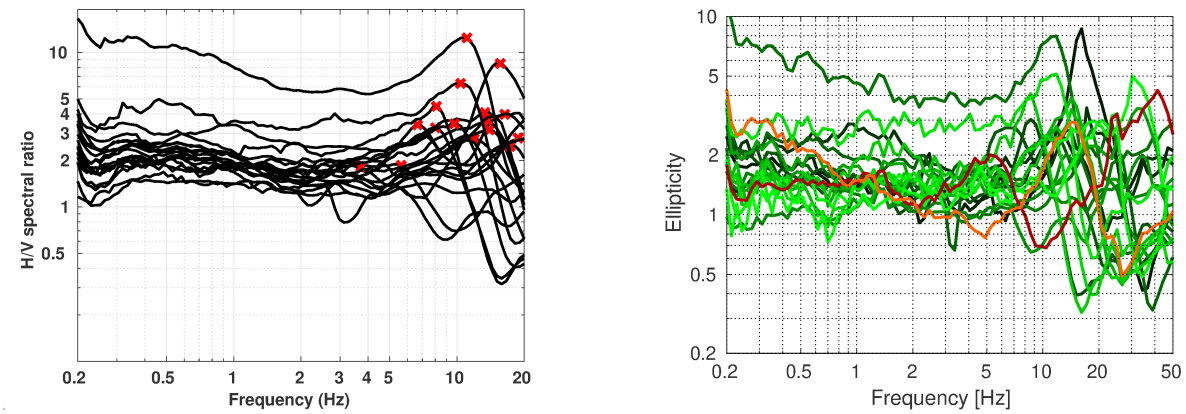

Figure 4: Left: Overview of the H/V measurements for the different stations of both array measurements. Right: RayDec ellipticities for all measurement stations. The orange curve belongs to station SWIM46, the central station of the arrays, and the red curve to station SWIM42, the station next to the permanent station SWIM.

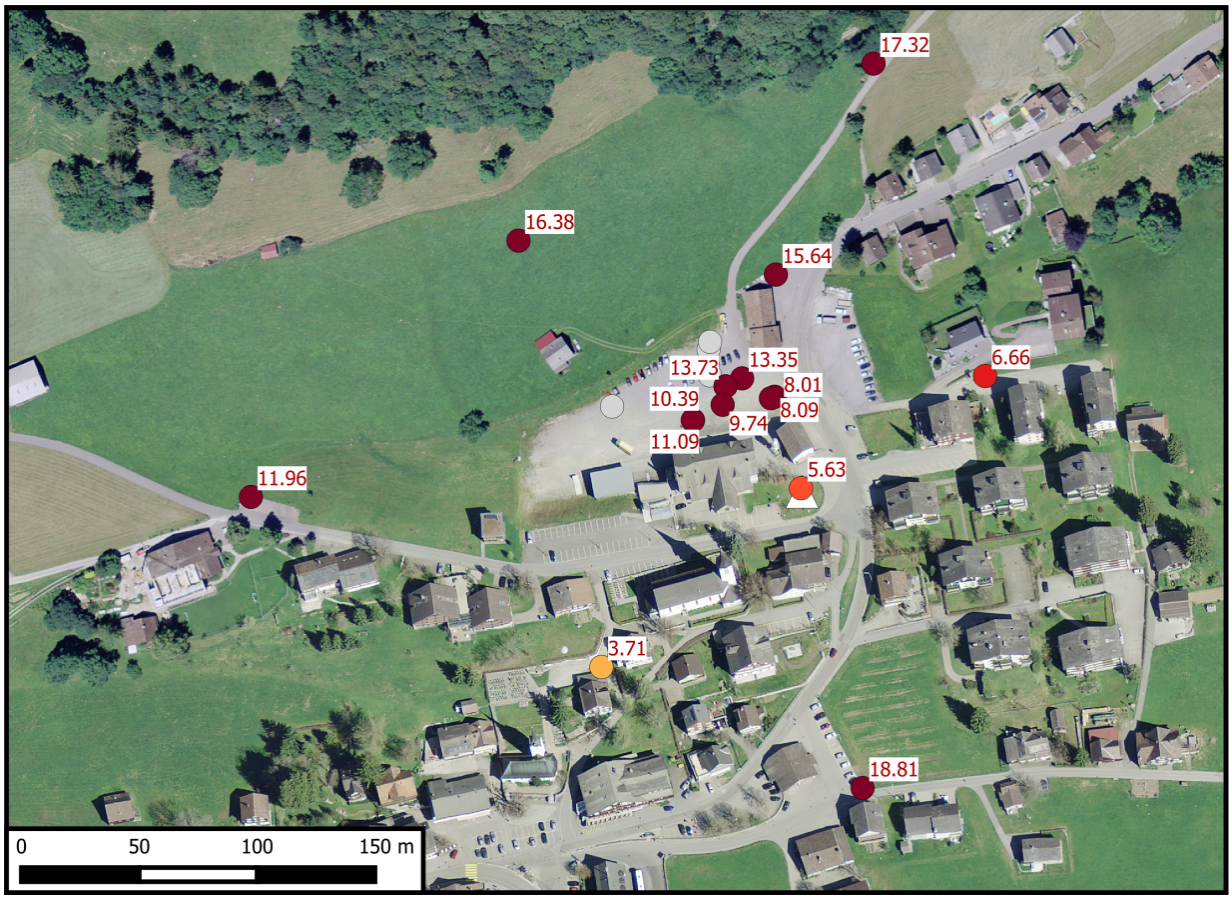

Figure 5: H/V peak frequencies for all stations of the array measurements. For the gray stations, no peak was picked. Source: Federal Office of Topography.

3.3 Polarization analysis

The polarization analysis was performed according to Burjánek et al. (2010) and Burjánek et al. (2012). The results for all stations reflect the variability of the underground in the area. The results for SWIM42, the station closest to SWIM, and SWIM46, the central station of array 1, are shown here.
For SWIM42, a predominant azimuth of 60°/240° is visible below 0.2 Hz. At higher frequencies, no 2-dimensional polarization effects are visible. For SWIM46, no polarization effects are visible as well.

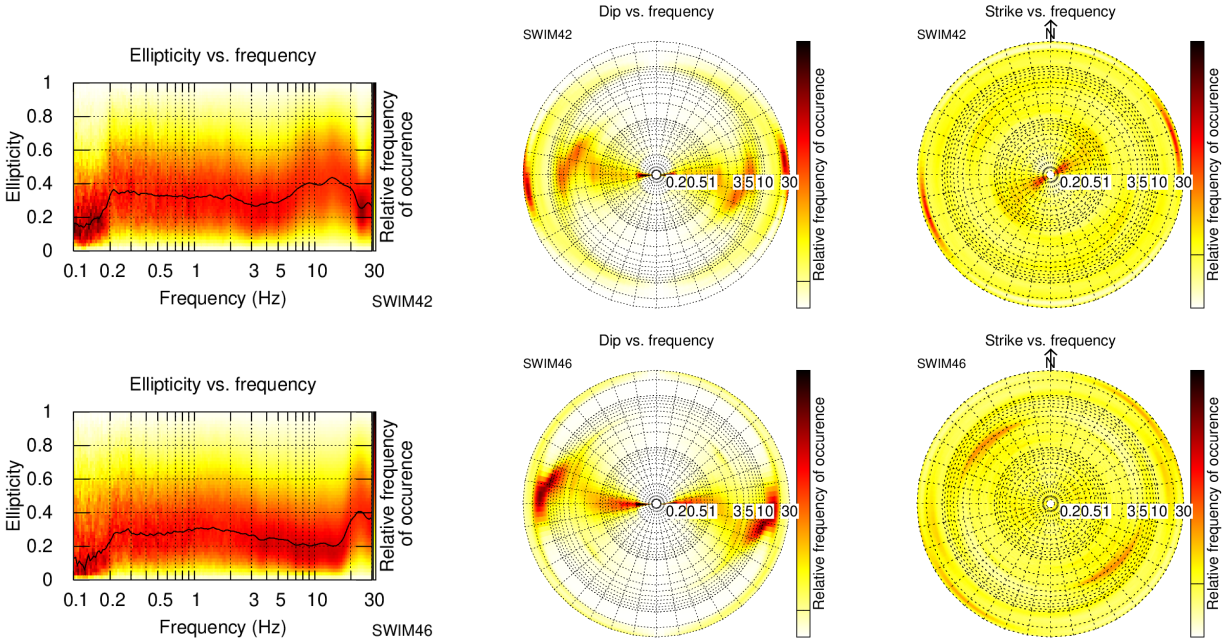

Figure 6: Polarization analysis of stations SWIM42 (top) and SWIM46 (bottom).

3.4 3-component high-resolution FK

The results of the 3-component high-resolution FK analysis (Poggi and Fäh, 2010) for the three arrays are shown in Fig. 7.
On the transverse component, corresponding to Love waves, we can identify a dispersion curve between 4.4 and 8.5 Hz for array 1, between 12.6 and 18.7 Hz for array 2 and between 15.6 and 37.1 Hz for array 3, but the curve for array 3 is not very clear.
On the vertical component, corresponding to Rayleigh waves, we can clearly identify one mode between 4.9 and 9.5 Hz for array 1, a relatively unclear curve between 16.7 and 18.0 Hz and between 23.8 and 26.6 Hz for array 2 and, also not very clear, between 19.3 and 28.1 Hz for array 3.
On the radial component, the results are also not very clear. For array 1, a dispersion curve can be picked between 4.9 and 6.0 Hz. For array 2, the picking is more clear and a curve is found between 12.1 and 16.8 Hz, while no curve can be identified for array 3.
The corresponding ellipticity curves of these modes will be compared with the single-station ellipticity curves at a later stage.

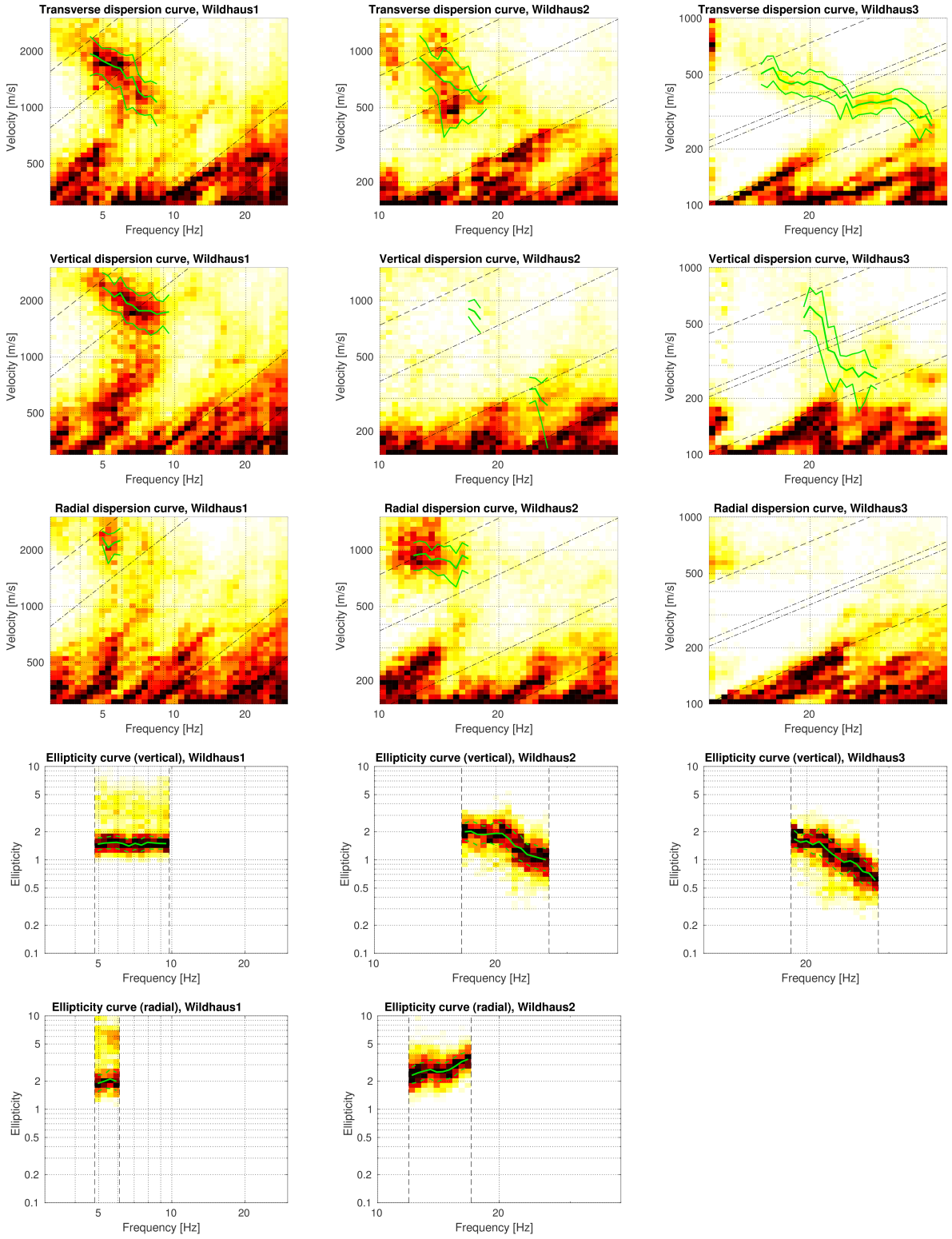

Figure 7: Dispersion curves obtained with the 3-component HRFK algorithm (Poggi and Fäh, 2010). From top to bottom, the dispersion curves for the transverse, vertical and radial components and the ellipticity curves for the vertical and radial components are shown for array 1 (left column), array 2 (central column) and array 3 (right column). The dashed and dotted black lines are the array resolution limits.

3.5 WaveDec

The results of the WaveDec (Maranò et al., 2012) processing are shown in Fig. 8. This technique estimates the properties of single or multiple waves simultaneously with a maximum likelihood approach. In order to improve the results, the parameter γ, which modifies the sharpness of the wave property estimation, has been tuned. Here, a value of $\gamma = 0.2$ was used, corresponding to a predominantly maximum likelihood estimation. Love wave dispersion curves are retrieved for all three arrays, between 3.5 and 11.5 Hz for array 1, between 10.4 and 20.6 Hz for array 2 and, less clear, between 15.1 and 26.1 Hz for array 3.
For Rayleigh waves, the results are less clear. No dispersion curve can be identified for array 1. For array 2, a dispersion curve is not very clear between 15.9 and 18.9 Hz. For array 3, a curve can be picked between 15.9 and 24.8 Hz.
The ellipticity angles for the picked Rayleigh wave dispersion curves are mostly positive for both arrays, corresponding to prograde particle motion.

3.6 SPAC

The SPAC (Aki, 1957) curves of the vertical components have been calculated using the M-SPAC (Bettig et al., 2001) technique implemented in geopsy. Rings with different radius ranges were defined previously and for all station pairs with distance inside this radius range, the cross-correlation was calculated over a wide frequency range. These cross-correlation curves are averaged for all station pairs of the respective ring and give the SPAC curves. The rings are defined in such a way that at least three station pairs contribute and that their connecting vectors have a good directional coverage.
The calculation was performed for array 1 and array 2. The respective SPAC curves are shown in Figs 9 and 10. As the retrieved SPAC curves have no good similarity with the theoretical Bessel functions in most cases, it was not possible to retrieve a dispersion curve.

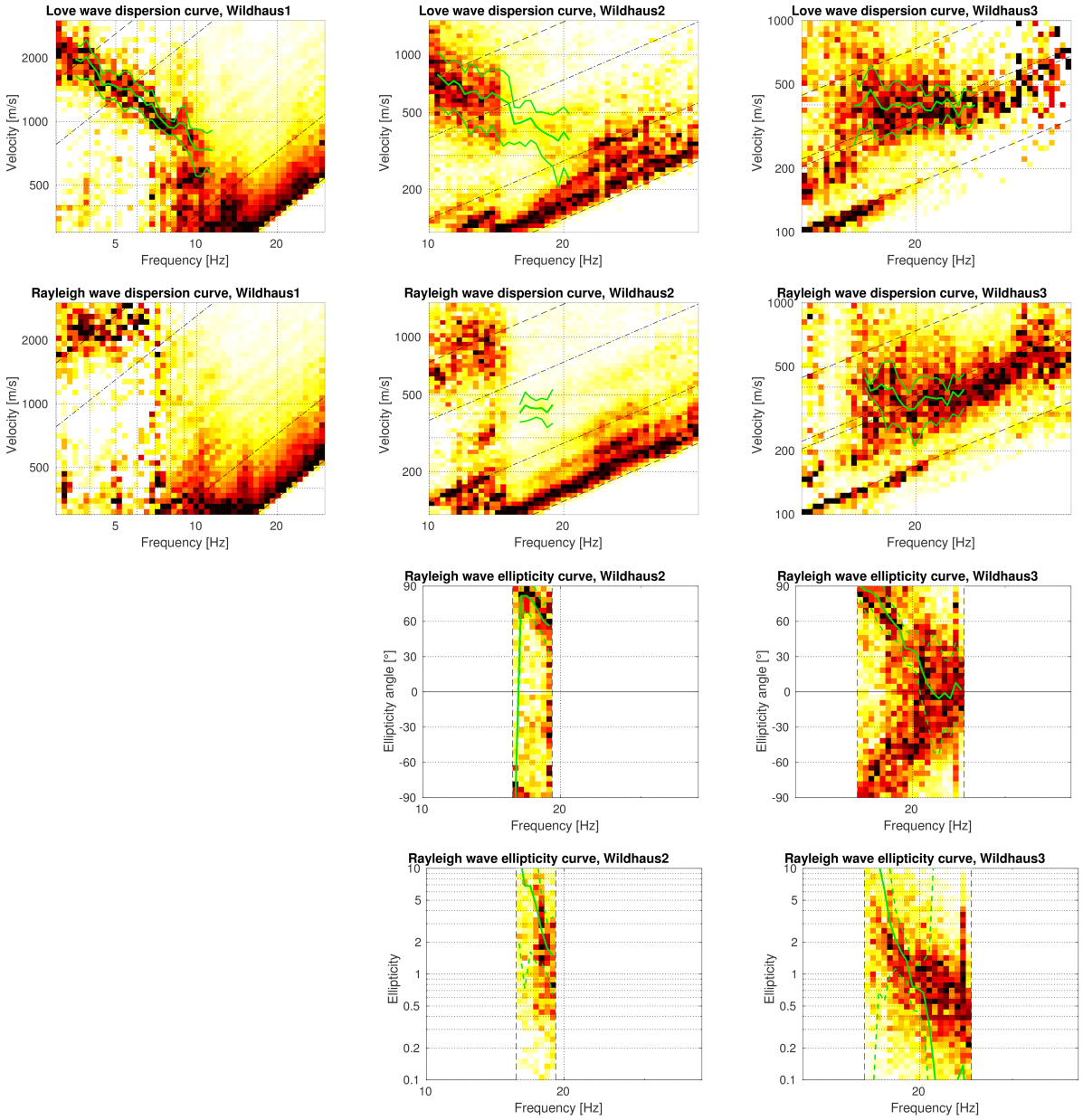

Figure 8: Love (top line) and Rayleigh (bottom line) wave dispersion curves obtained with the WaveDec technique (Maranò et al., 2012) for array 3 (left) and array 4 (right). The dashed lines indicate the theoretical array resolution limits.

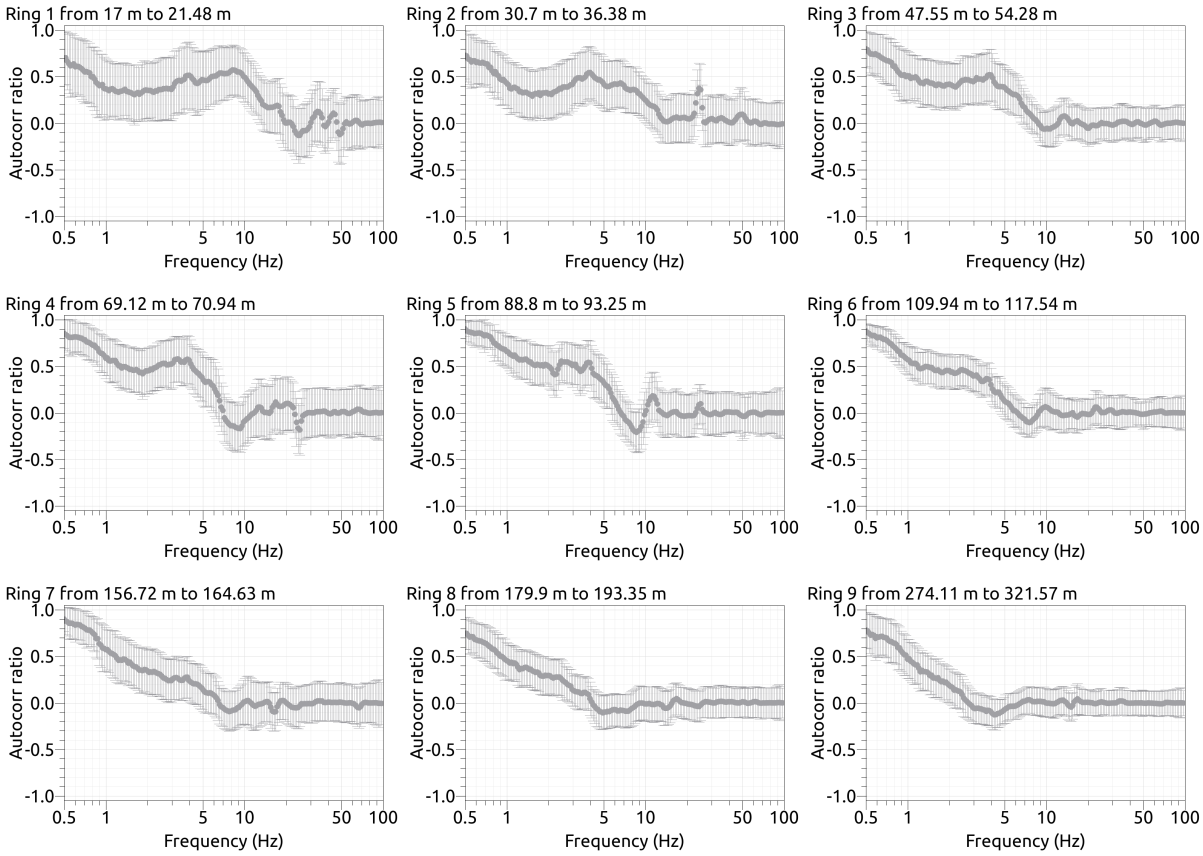

Figure 9: SPAC curves for nine rings of array 1.

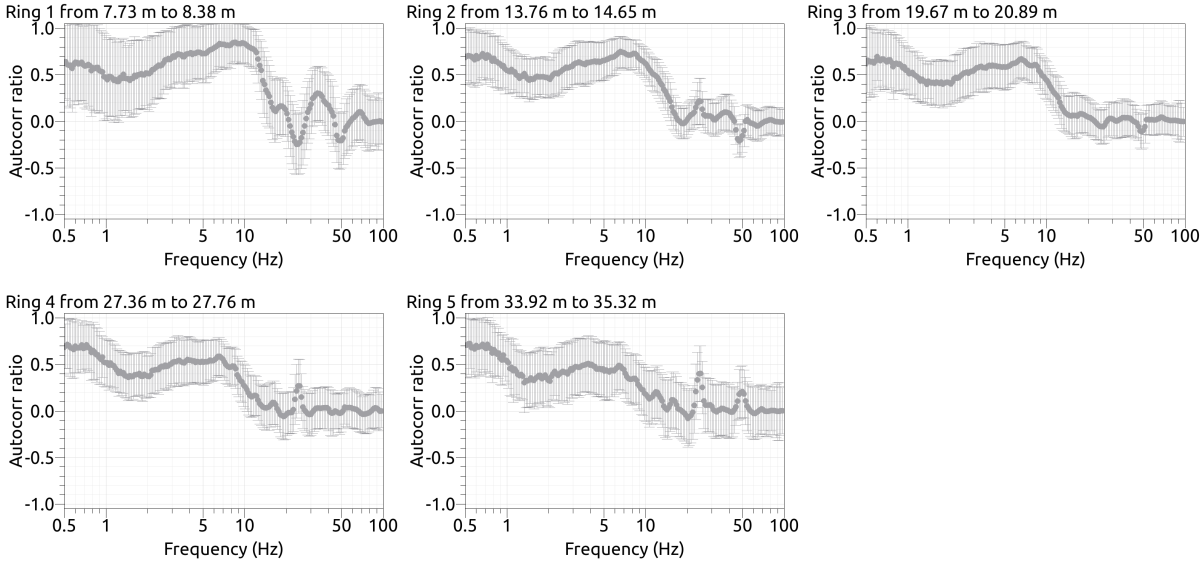

Figure 10: SPAC curves for five rings of array 2.

3.7 Summary

Fig. 11 gives an overview of the dispersion and ellipticity curves determined by the different methods.
For Love waves, the WaveDec curves for the three arrays fit together. The HRFK curves are in relatively good agreement with them, but show slightly higher velocities for arrays 1 and 2.
For Rayleigh waves, no clear and continuous dispersion curve can be retrieved. The curves from array 1 are separated by a frequency gap from the other curves. The WaveDec curves were not clear to pick and are also not completely consistent with the HRFK curves. Nevertheless, the HRFK curves can be combined to a continuous dispersion curve.
The ellipticity curves retrieved by RayDec for the station next to the permanent station SWIM (SWIM42) and the array center (SWIM46) highlight the variability of the underground structure. While SWIM46 shows a peak frequency of about 14.3 Hz, SWIM42 shows peaks at 5.63 and 41.4 Hz. In that respect, the ellipticity curves from the HRFK processing are in agreement with these ellipticity curves. The WaveDec curves for arrays 2 and 3 show a singularity at about 14 Hz and are in that way in good agreement with SWIM46. As these two small-scale arrays are located on the parking lot and SWIM46 is in the array center, this agreement makes sense. These results also indicate that the results of arrays 2 and 3 are not representative for the permanent station, which is close to SIWM42.

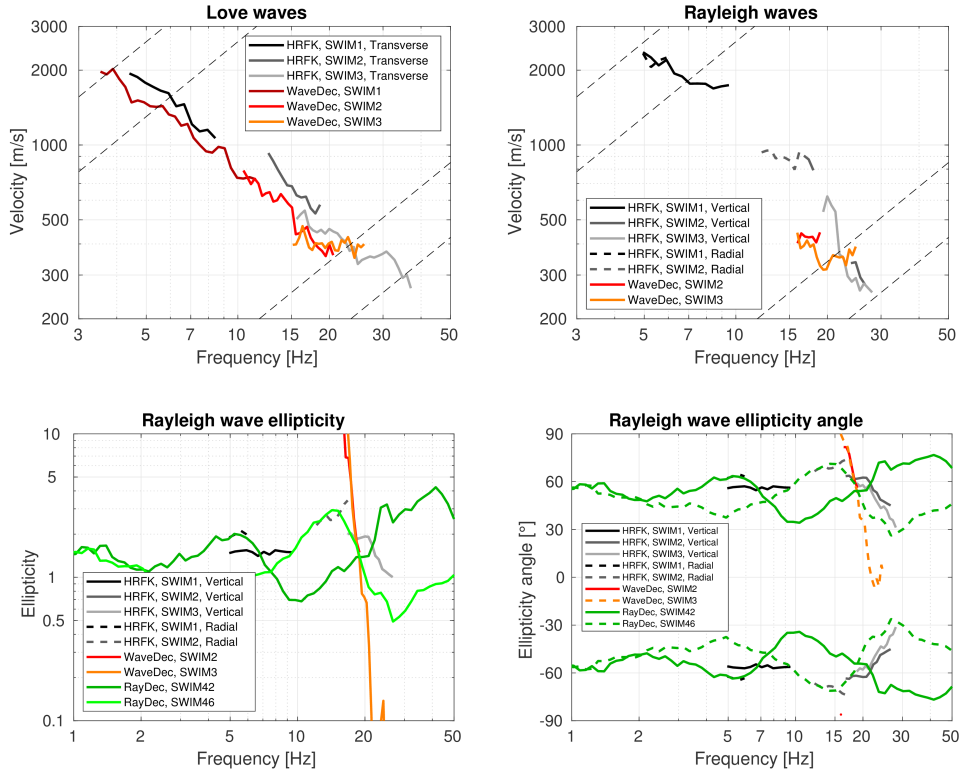

Figure 11: Overview of the Love and Rayleigh wave dispersion curves as well as the ellipticity and ellipticity angle curves for both arrays. The dashed lines indicate the theoretical resolution limits of array 3 (high frequencies) and array 1 (low frequencies). The RayDec ellipticity curves correspond to stations SWIM42 and SWIM46.

4 Data inversion

4.1 Inversion targets

As the measured dispersion and ellipticity curves for the center of the array and close to the permanent station SWIM were different, we performed inversions using two different targets.
The first target, based on data valid close to the permanent station, excludes the higher-frequency dispersion curves measured by arrays 2 and 3. The used data are indicated in Table 2 and shown in the first line of Fig. 12. The WaveDec dispersion curve of array 1 is used for Love waves, the vertical HRFK curve of array 1 for Rayleigh waves. Additionally, a wide ellipticity angle curve based on the RayDec ellipticity curve of SWIM42 and assuming retrograde particle motion over the whole frequency range, i.e. excluding singularities, is used.
The second target includes the data of arrays 2 and 3 and is therefore valid for the center of the arrays. Its properties are indicated in Table 3 and shown in the bottom line of Fig. 12. The WaveDec dispersion curves of arrays 1 and 2 and the transverse HRFK curve of array 3 are used for the Love waves. For the Rayleigh waves, the vertical HRFK curves of arrays 1, 2, and 3 are used. The RayDec ellipticity angle for station SWIM46 is used at lower and higher frequencies, assuming retrograde particle motion, and the WaveDec ellipticity angle measured with array 3 is used in the intermediate range, where it is prograde. This parameterization forces a singularity with a change of the sense of rotation between 12 and 16 Hz.

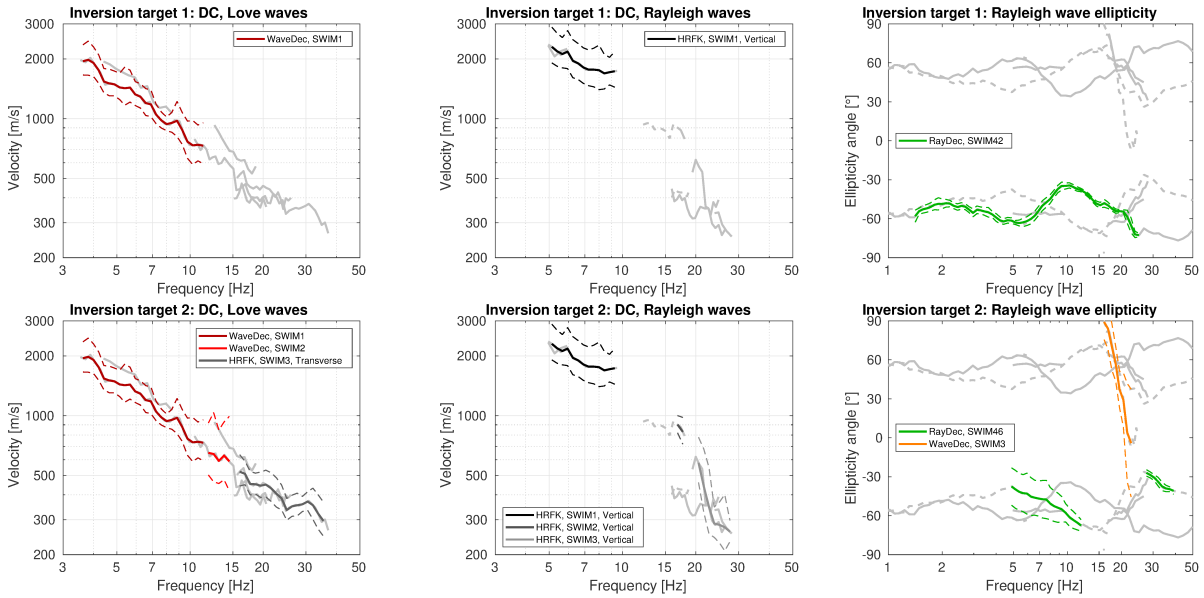

Figure 12: Overview of the dispersion and ellipticity angle curves used as targets 1 and 2 for the different inversions.

Table 2: List of the different data curves used as target 1.

Array	Method	Wave type	Mode	Curve type	Frequency range [Hz]
1	WaveDec	Love	fundamental	dispersion	3.62 - 11.32
1	HRFK (V)	Rayleigh	fundamental	dispersion	5.12 - 9.29
	RayDec (SWIM42)	Rayleigh	fundamental	ellipticity angle (-)	1.41 - 25.00

Table 3: List of the different data curves used as target 2.

Array	Method	Wave type	Mode	Curve type	Frequency range [Hz]
1	WaveDec	Love	fundamental	dispersion	3.62 - 11.32
2	WaveDec	Love	fundamental	dispersion	11.89 - 14.50
3	HRFK (T)	Love	fundamental	dispersion	16.00 - 35.36
1	HRFK (V)	Rayleigh	fundamental	dispersion	5.12 - 9.29
2	HRFK (V)	Rayleigh	fundamental	dispersion	16.82 - 17.68
3	HRFK (V)	Rayleigh	fundamental	dispersion	20.50 - 27.60
	RayDec (SWIM46)	Rayleigh	fundamental	ellipticity angle (-)	4.87 - 11.90
3	WaveDec	Rayleigh	fundamental	ellipticity angle	16.00 - 22.64
	RayDec (SWIM46)	Rayleigh	fundamental	ellipticity angle (-)	27.59 - 39.04

4.2 Inversion parameterization

For the inversion, six different parameterizations were used in total. The first five have free values of the depths and velocities of the different layers, ranging from four to eight layers (including half-space). The last parameterization has fixed layer depths and consists of 19 layers in total. The P-wave velocities are allowed to vary up to 5000 m/s. The S-wave velocities are allowed to range from 30 to 3500 m/s. The deepest boundaries are allowed at a depth of 300 m maximum (200 m for the fixed-depth approach). The density is fixed to 2300 kg/m^3 for the lowest layer, to 1900 kg/m^3 for the superficial layer (or the first three layers in the fixed-layer case) and to 2100 kg/m^3 for all other layers. No low-velocity zones are allowed.

4.3 Inversion results

For each parameterization, 20 different runs were performed, but only the one giving the best minimum misfit was kept. In Table 4, the obtained minimum misfit values for these inversions are shown. In order to assure a good convergence of the solution, each inversion run for the 4-layer parameterization produced around 100 000 total models, for the 5-layer parameterizations around 150 000 models and for all other inversions around 200 000 models. The results of the inversions SWIM4l1 to SWIMfix1 of target 1 are shown in Figs 13 - 18, for the inversions SWIM4l2 to SWIMfix2 using target 2 in Figs 19 - 24.

For target 1, the 4-layer inversion results in a minimum misfit of 0.9, significantly higher than for the other inversions. We conclude that this parameterization is not sufficient to fit the data well. The other inversions fit the dispersion data in a better way. The ellipticity curve is in general fitted the best. Also the Love wave dispersion curve is well fitted, but the Rayleigh wave dispersion curve, which also had large uncertainties from the measurement, is not that well fitted in all inversions.
Also for target 2, the 4-layer inversion has a much higher minimum misfit value than the other parameterizations, which fit the data in a comparable way. Also for these inversions, the Love wave dispersion and Rayleigh wave ellipticity curves are well fitted and the fit for the Rayleigh wave dispersion curve is worse.

Table 4: List of inversions

Inversion	Number of layers	Number of models	Minimum misfit
SWIM4l1	4	100 005	0.900
SWIM5l1	5	150 040	0.775
SWIM6l1	6	200 040	0.611
SWIM7l1	7	200 062	0.748
SWIM8l1	8	200 079	0.732
SWIMfix1	19	200 040	0.818
SWIM4l2	4	100 048	1.036
SWIM5l2	5	150 000	0.600
SWIM6l2	6	199 999	0.583
SWIM7l2	7	200 013	0.582
SWIM8l2	8	200 007	0.603
SWIMfix2	19	200 025	0.649

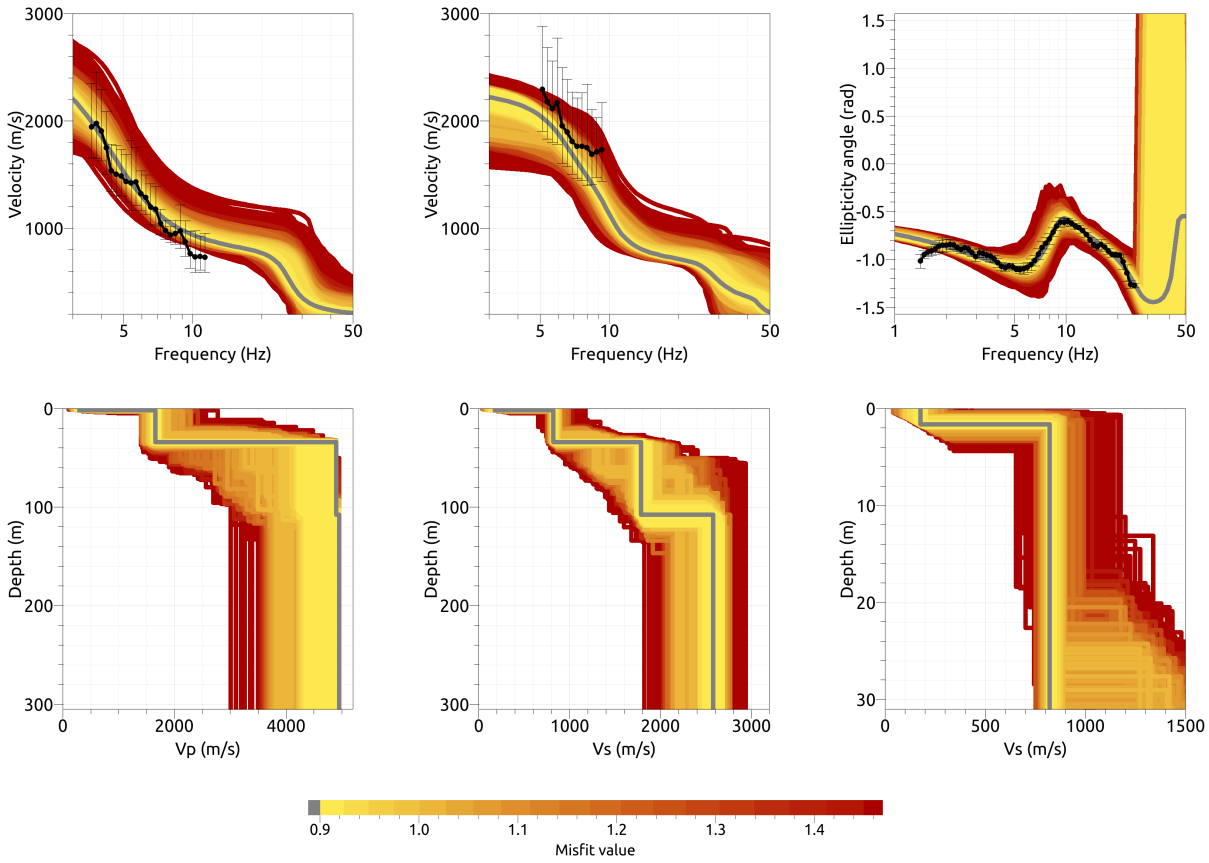

Figure 13: Inversion SWIM4l1. Top line: Dispersion curves for Love waves (left) and Rayleigh waves (center) and Rayleigh wave ellipticity angle (right) of the respective fundamental modes. Bottom line: P-wave velocity profiles (left), S-wave velocity profiles (center and zoom on the upper 30 m on the right). All generated models are plotted on top of each other in the color corresponding to the respective misfit value. The black dots with error bars indicate the data points used for the inversion, the gray line indicates the best-fitting model. In the ellipticity angle plot, the light gray dots and error bars indicate the ellipticity values of targets 2 and 3, which where not used for the inversion here.

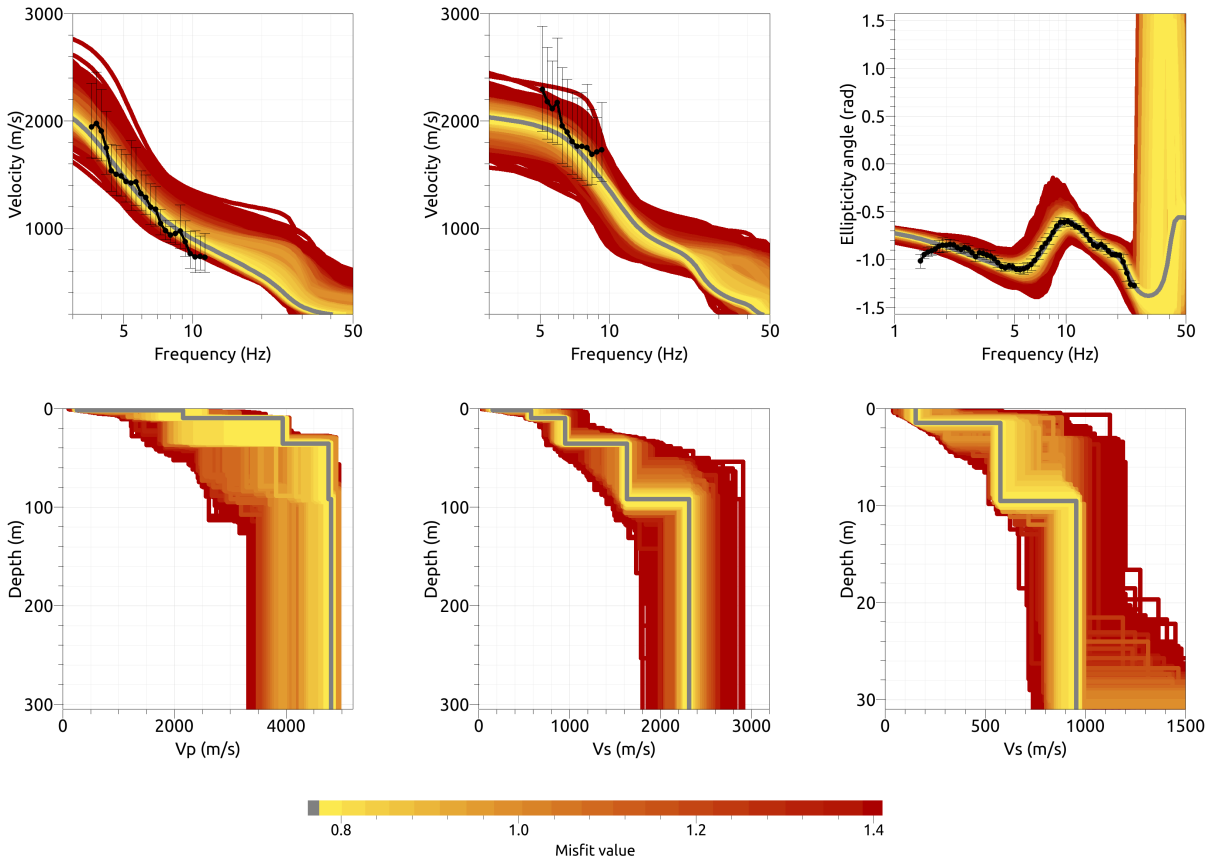

Figure 14: Inversion SWIM5l1. Top line: Dispersion curves for Love waves (left) and Rayleigh waves (center) and Rayleigh wave ellipticity angle (right) of the respective fundamental modes. Bottom line: P-wave velocity profiles (left), S-wave velocity profiles (center and zoom on the upper 30 m on the right). All generated models are plotted on top of each other in the color corresponding to the respective misfit value. The black dots with error bars indicate the data points used for the inversion, the gray line indicates the best-fitting model. In the ellipticity angle plot, the light gray dots and error bars indicate the ellipticity values of targets 2 and 3, which where not used for the inversion here.

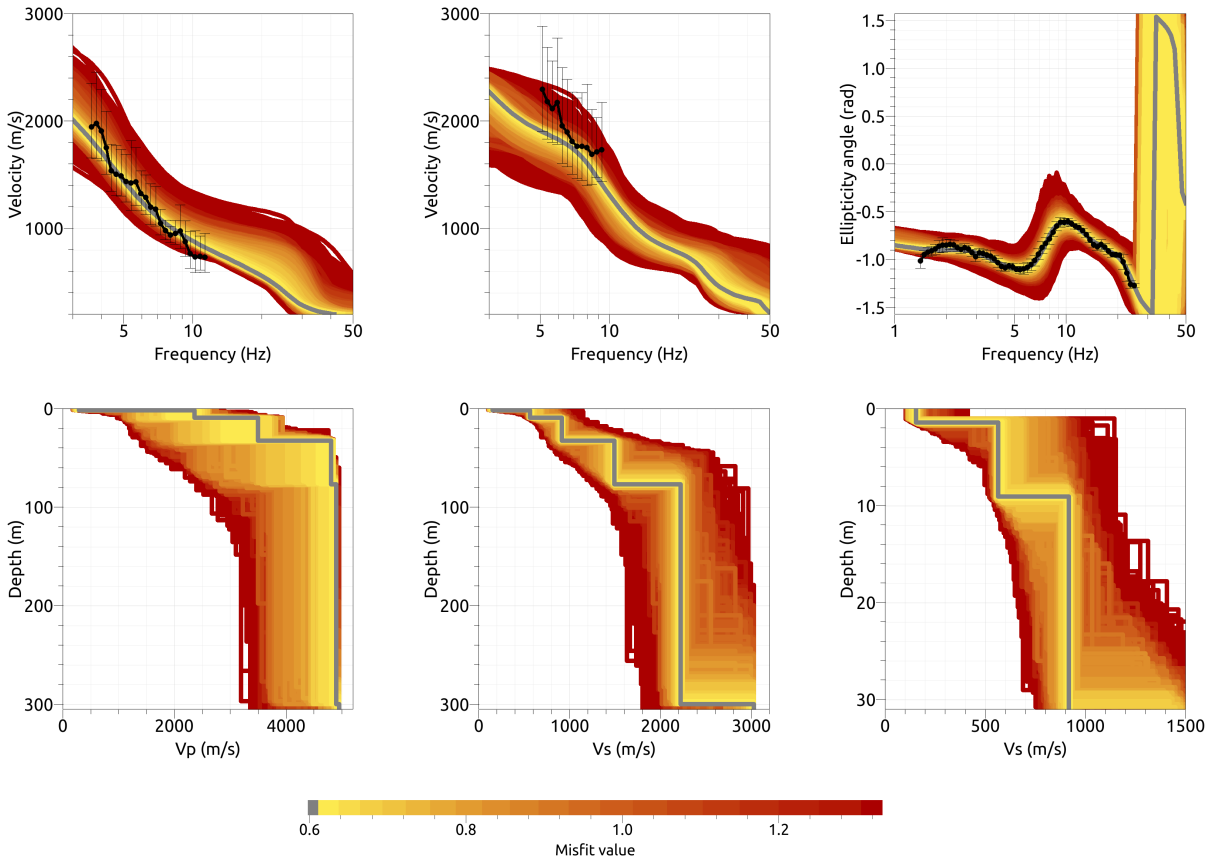

Figure 15: Inversion SWIM6l1. Top line: Dispersion curves for Love waves (left) and Rayleigh waves (center) and Rayleigh wave ellipticity angle (right) of the respective fundamental modes. Bottom line: P-wave velocity profiles (left), S-wave velocity profiles (center and zoom on the upper 30 m on the right). All generated models are plotted on top of each other in the color corresponding to the respective misfit value. The black dots with error bars indicate the data points used for the inversion, the gray line indicates the best-fitting model. In the ellipticity angle plot, the light gray dots and error bars indicate the ellipticity values of targets 2 and 3, which where not used for the inversion here.

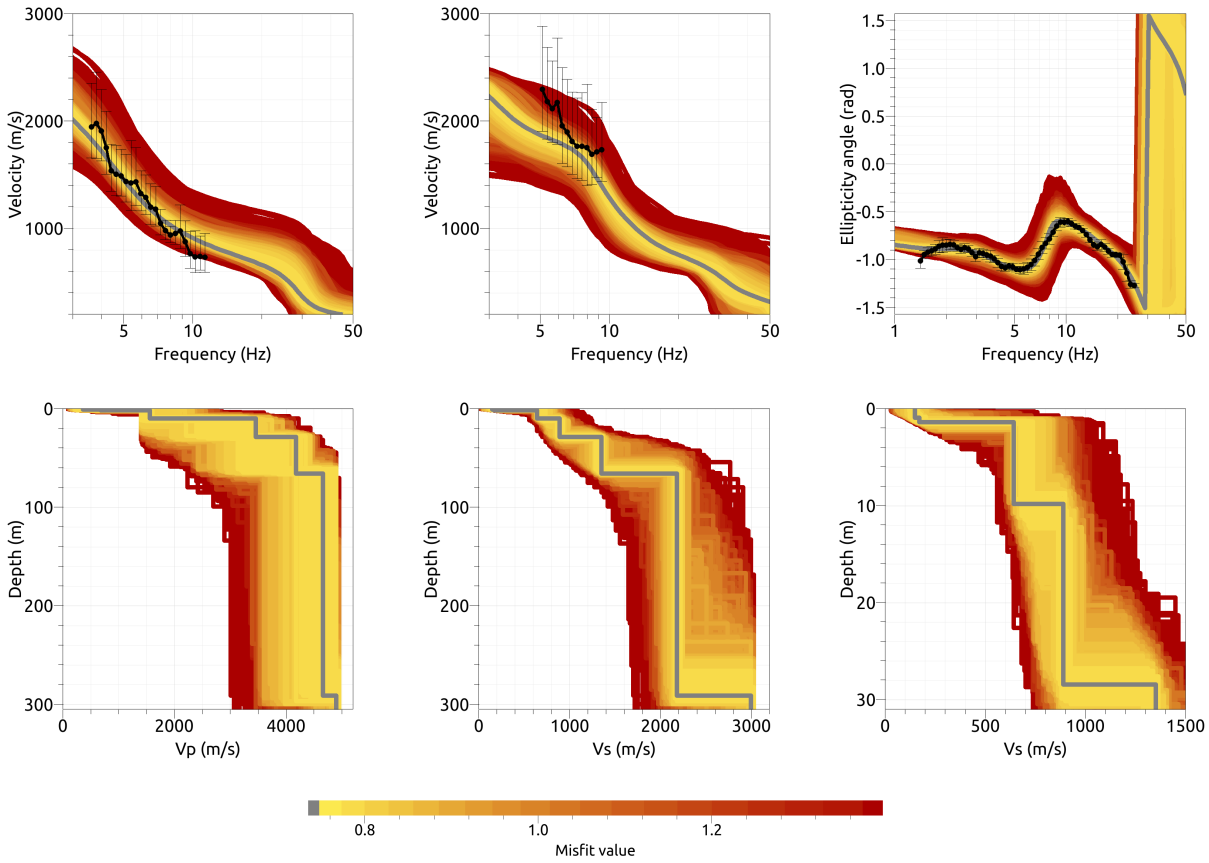

Figure 16: Inversion SWIM7l1. Top line: Dispersion curves for Love waves (left) and Rayleigh waves (center) and Rayleigh wave ellipticity angle (right) of the respective fundamental modes. Bottom line: P-wave velocity profiles (left), S-wave velocity profiles (center and zoom on the upper 30 m on the right). All generated models are plotted on top of each other in the color corresponding to the respective misfit value. The black dots with error bars indicate the data points used for the inversion, the gray line indicates the best-fitting model. In the ellipticity angle plot, the light gray dots and error bars indicate the ellipticity values of targets 2 and 3, which where not used for the inversion here.

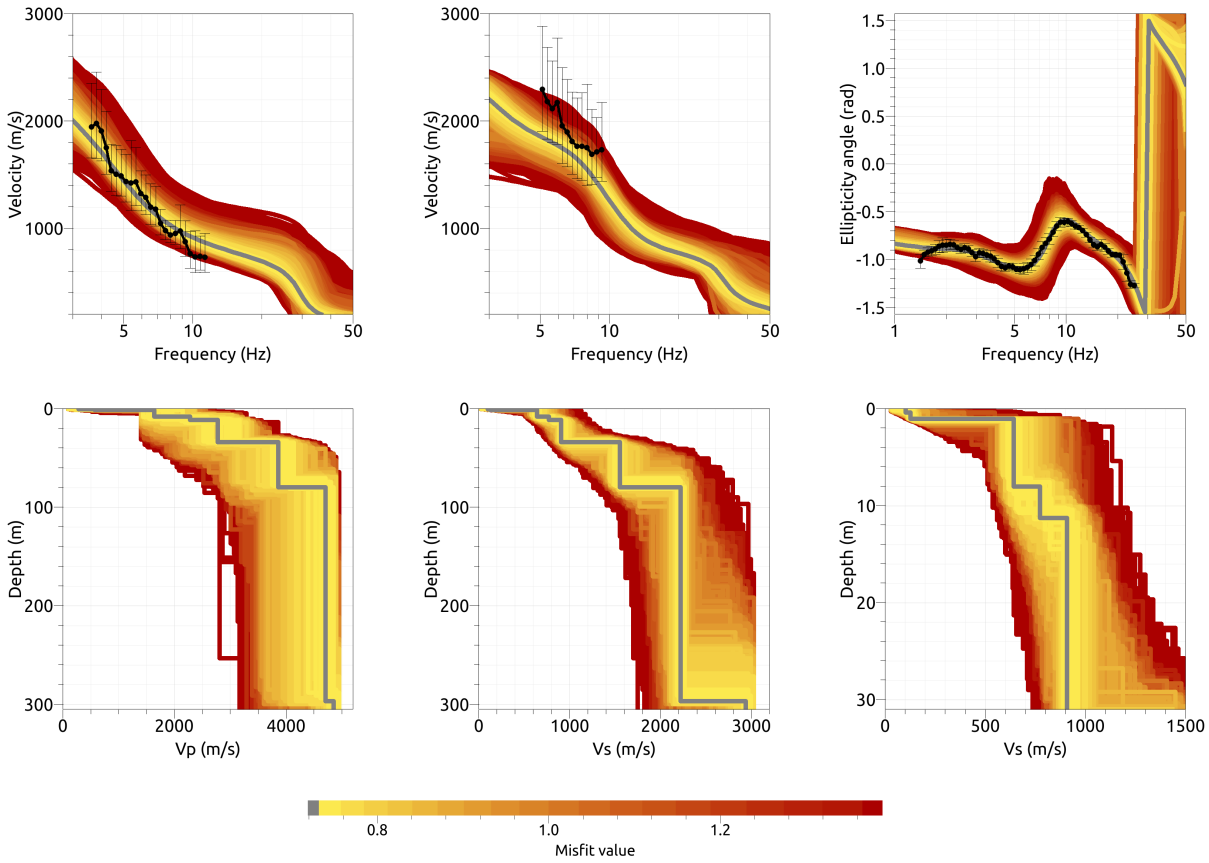

Figure 17: Inversion SWIM8l1. Top line: Dispersion curves for Love waves (left) and Rayleigh waves (center) and Rayleigh wave ellipticity angle (right) of the respective fundamental modes. Bottom line: P-wave velocity profiles (left), S-wave velocity profiles (center and zoom on the upper 30 m on the right). All generated models are plotted on top of each other in the color corresponding to the respective misfit value. The black dots with error bars indicate the data points used for the inversion, the gray line indicates the best-fitting model. In the ellipticity angle plot, the light gray dots and error bars indicate the ellipticity values of targets 2 and 3, which where not used for the inversion here.

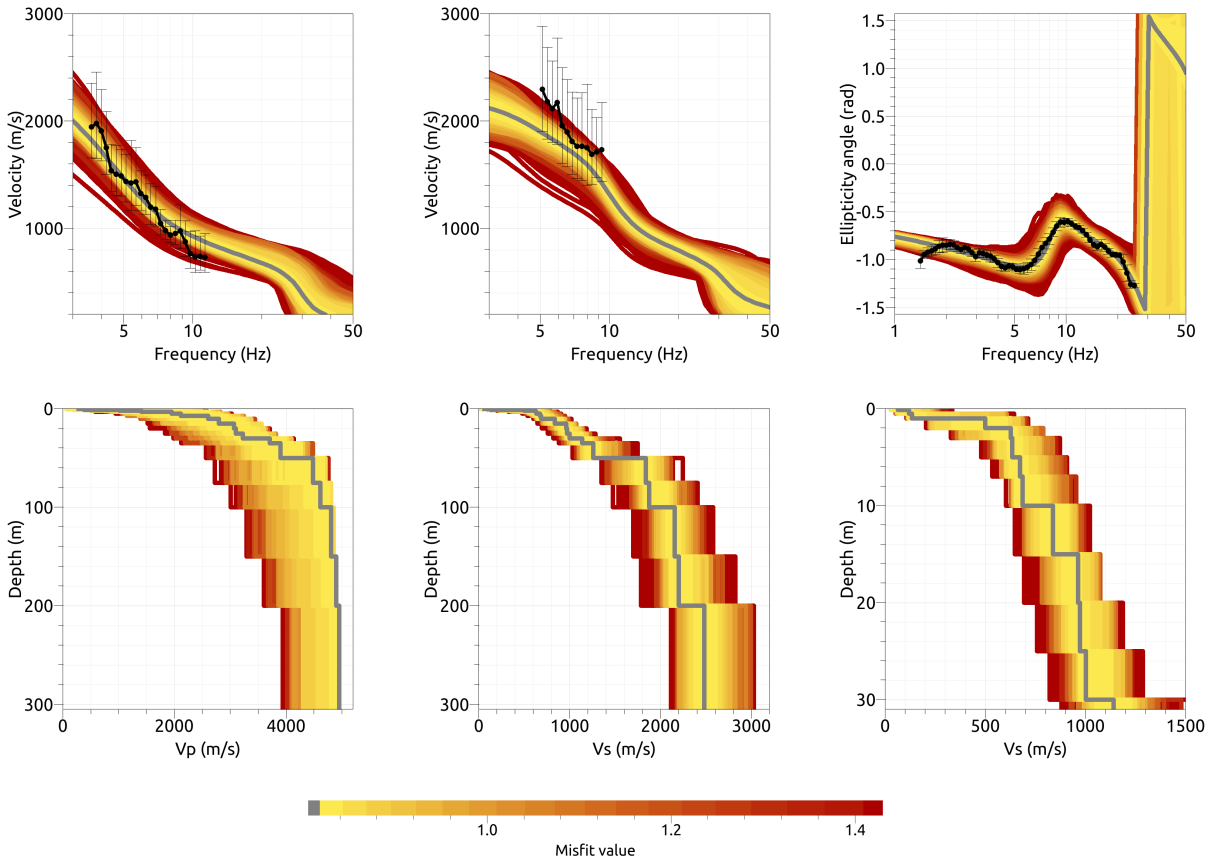

Figure 18: Inversion SWIMfix1. Top line: Dispersion curves for Love waves (left) and Rayleigh waves (center) and Rayleigh wave ellipticity angle (right) of the respective fundamental modes. Bottom line: P-wave velocity profiles (left), S-wave velocity profiles (center and zoom on the upper 30 m on the right). All generated models are plotted on top of each other in the color corresponding to the respective misfit value. The black dots with error bars indicate the data points used for the inversion, the gray line indicates the best-fitting model. In the ellipticity angle plot, the light gray dots and error bars indicate the ellipticity values of targets 2 and 3, which where not used for the inversion here.

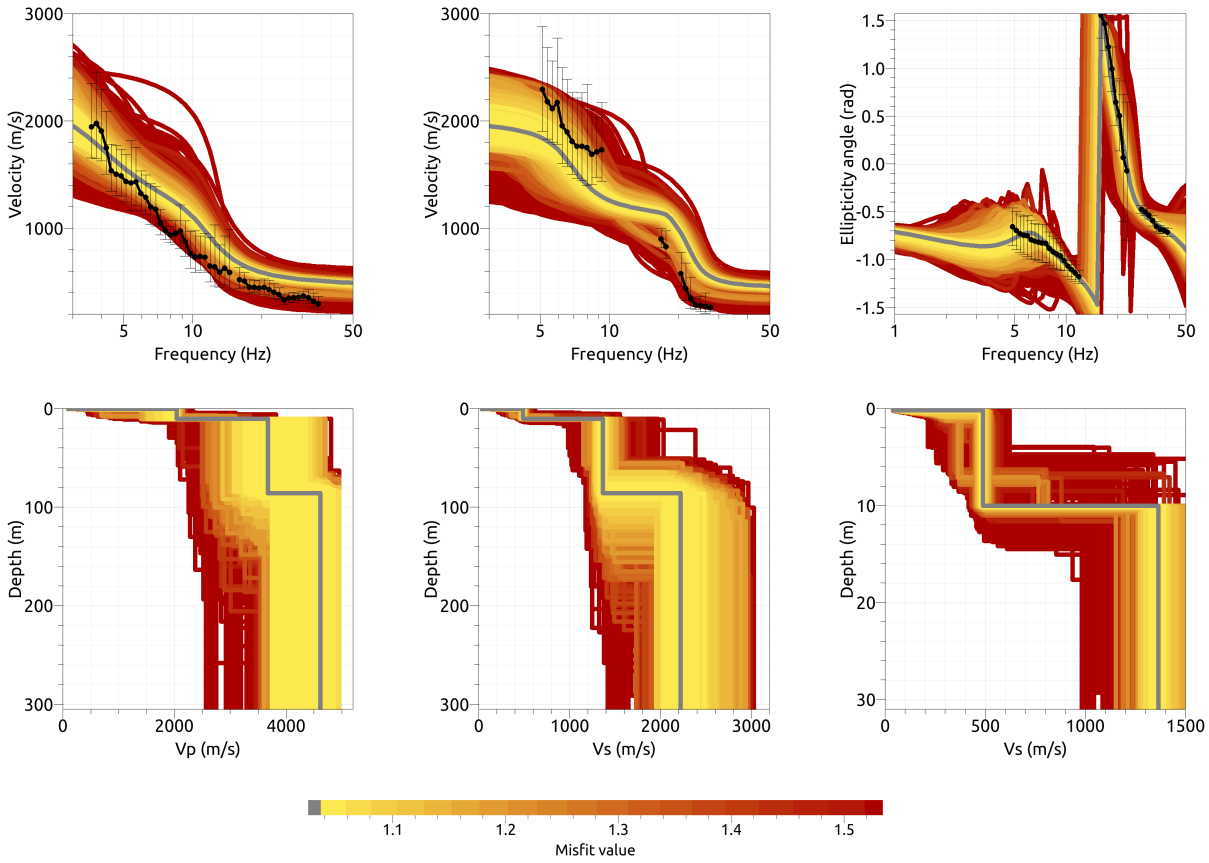

Figure 19: Inversion SWIM4l2. Top line: Dispersion curves for Love waves (left) and Rayleigh waves (center) and Rayleigh wave ellipticity angle (right) of the respective fundamental modes. Bottom line: P-wave velocity profiles (left), S-wave velocity profiles (center and zoom on the upper 30 m on the right). All generated models are plotted on top of each other in the color corresponding to the respective misfit value. The black dots with error bars indicate the data points used for the inversion, the gray line indicates the best-fitting model. In the ellipticity angle plot, the light gray dots and error bars indicate the ellipticity values of targets 2 and 3, which where not used for the inversion here.

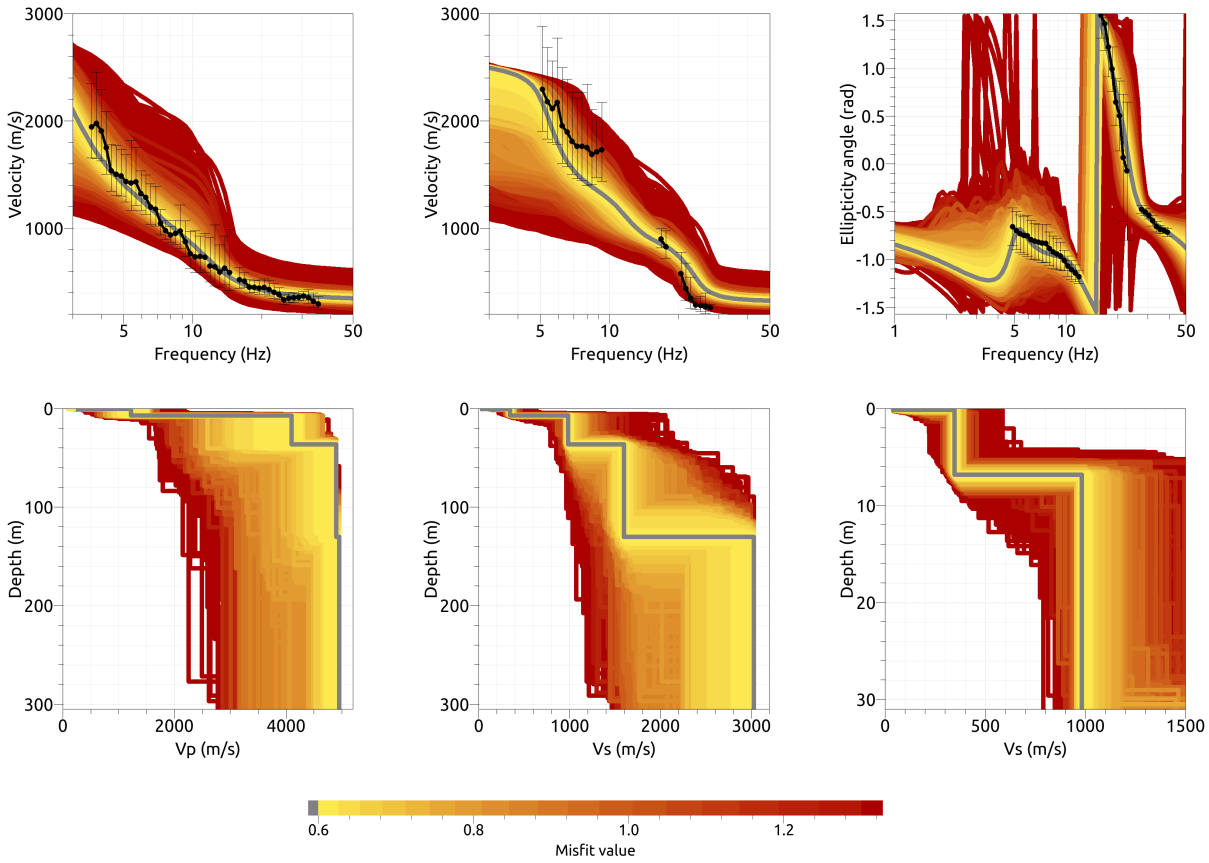

Figure 20: Inversion SWIM5l2. Top line: Dispersion curves for Love waves (left) and Rayleigh waves (center) and Rayleigh wave ellipticity angle (right) of the respective fundamental modes. Bottom line: P-wave velocity profiles (left), S-wave velocity profiles (center and zoom on the upper 30 m on the right). All generated models are plotted on top of each other in the color corresponding to the respective misfit value. The black dots with error bars indicate the data points used for the inversion, the gray line indicates the best-fitting model. In the ellipticity angle plot, the light gray dots and error bars indicate the ellipticity values of targets 2 and 3, which where not used for the inversion here.

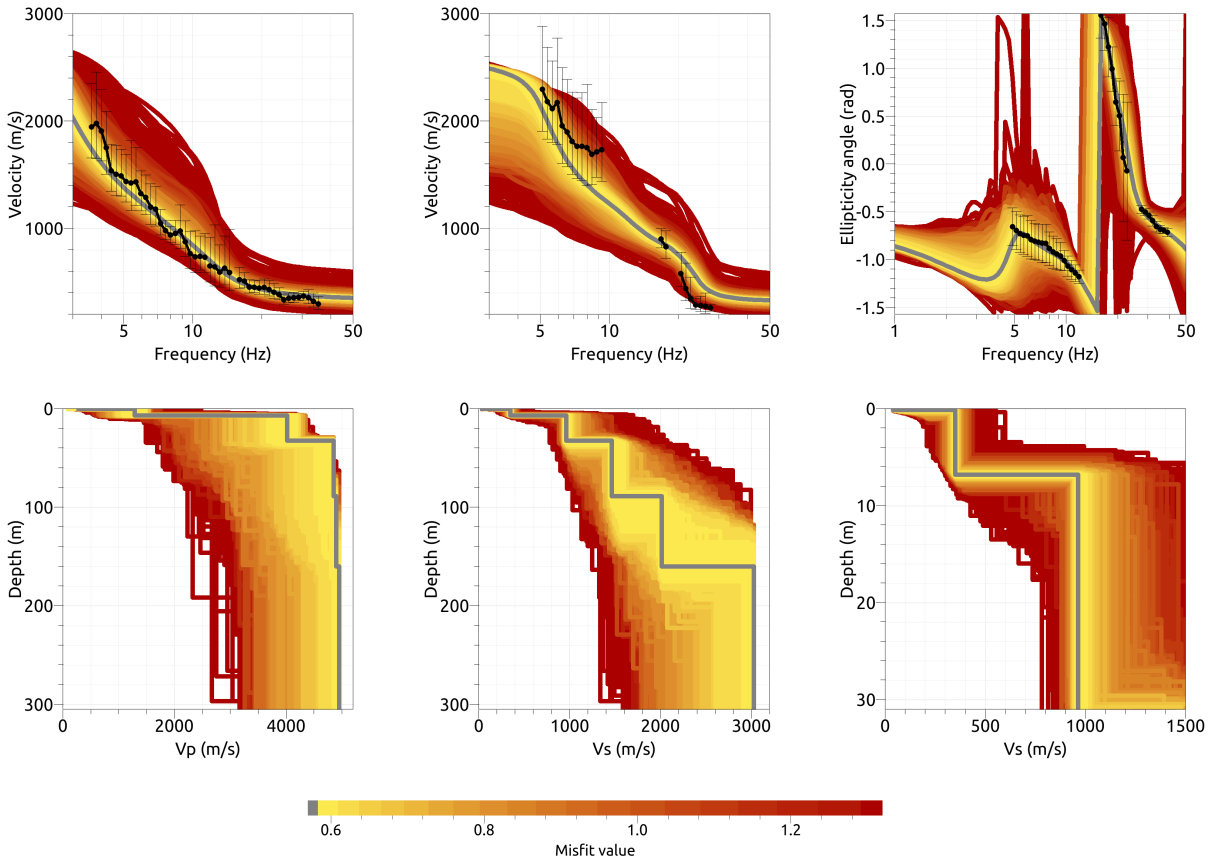

Figure 21: Inversion SWIM6l2. Top line: Dispersion curves for Love waves (left) and Rayleigh waves (center) and Rayleigh wave ellipticity angle (right) of the respective fundamental modes. Bottom line: P-wave velocity profiles (left), S-wave velocity profiles (center and zoom on the upper 30 m on the right). All generated models are plotted on top of each other in the color corresponding to the respective misfit value. The black dots with error bars indicate the data points used for the inversion, the gray line indicates the best-fitting model. In the ellipticity angle plot, the light gray dots and error bars indicate the ellipticity values of targets 2 and 3, which where not used for the inversion here.

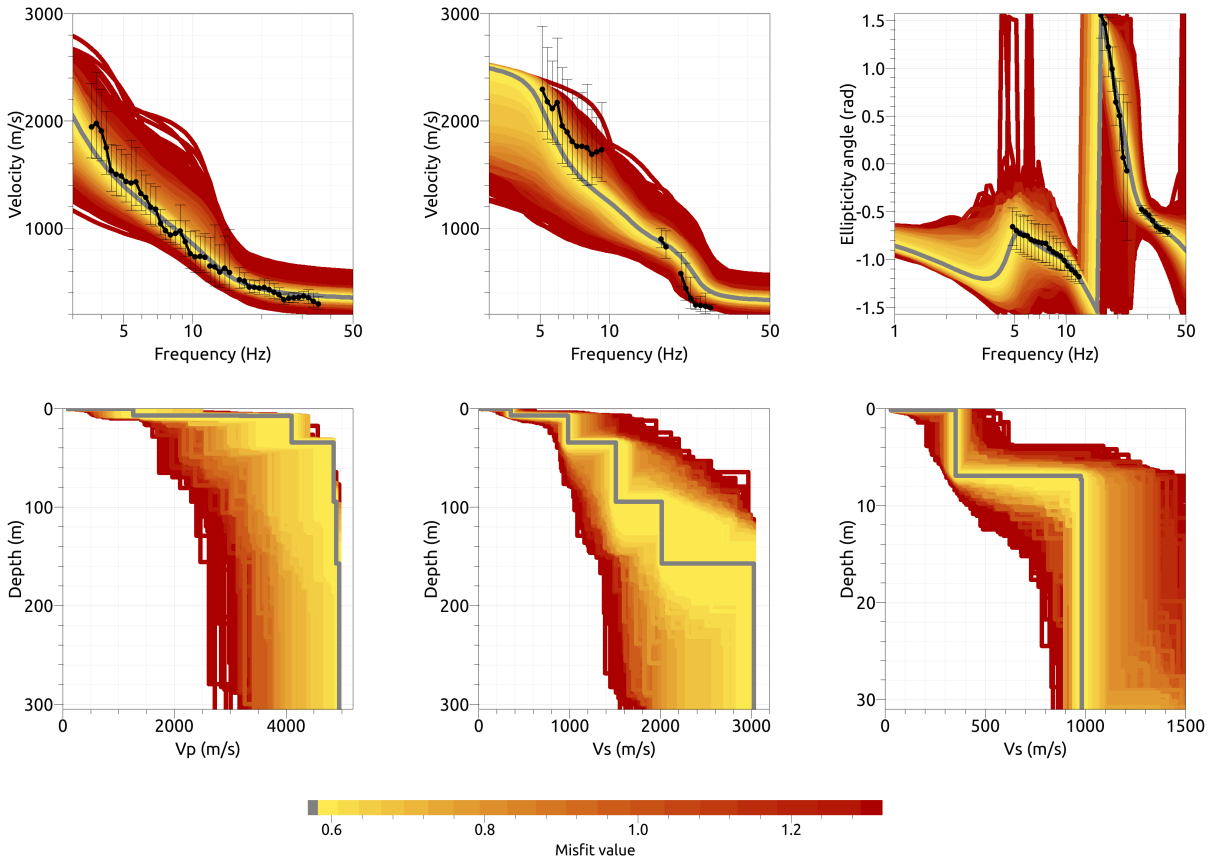

Figure 22: Inversion SWIM7l2. Top line: Dispersion curves for Love waves (left) and Rayleigh waves (center) and Rayleigh wave ellipticity angle (right) of the respective fundamental modes. Bottom line: P-wave velocity profiles (left), S-wave velocity profiles (center and zoom on the upper 30 m on the right). All generated models are plotted on top of each other in the color corresponding to the respective misfit value. The black dots with error bars indicate the data points used for the inversion, the gray line indicates the best-fitting model. In the ellipticity angle plot, the light gray dots and error bars indicate the ellipticity values of targets 2 and 3, which where not used for the inversion here.

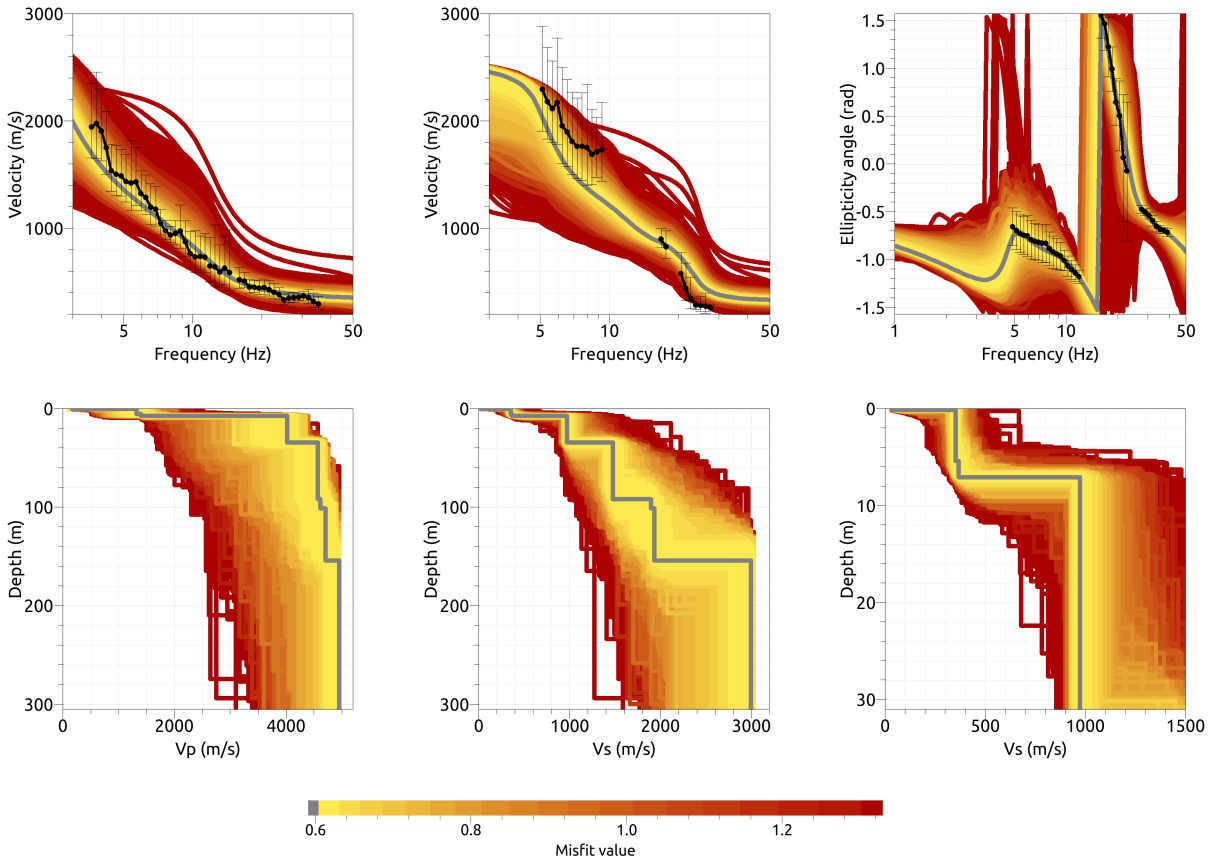

Figure 23: Inversion SWIM8l2. Top line: Dispersion curves for Love waves (left) and Rayleigh waves (center) and Rayleigh wave ellipticity angle (right) of the respective fundamental modes. Bottom line: P-wave velocity profiles (left), S-wave velocity profiles (center and zoom on the upper 30 m on the right). All generated models are plotted on top of each other in the color corresponding to the respective misfit value. The black dots with error bars indicate the data points used for the inversion, the gray line indicates the best-fitting model. In the ellipticity angle plot, the light gray dots and error bars indicate the ellipticity values of targets 2 and 3, which where not used for the inversion here.

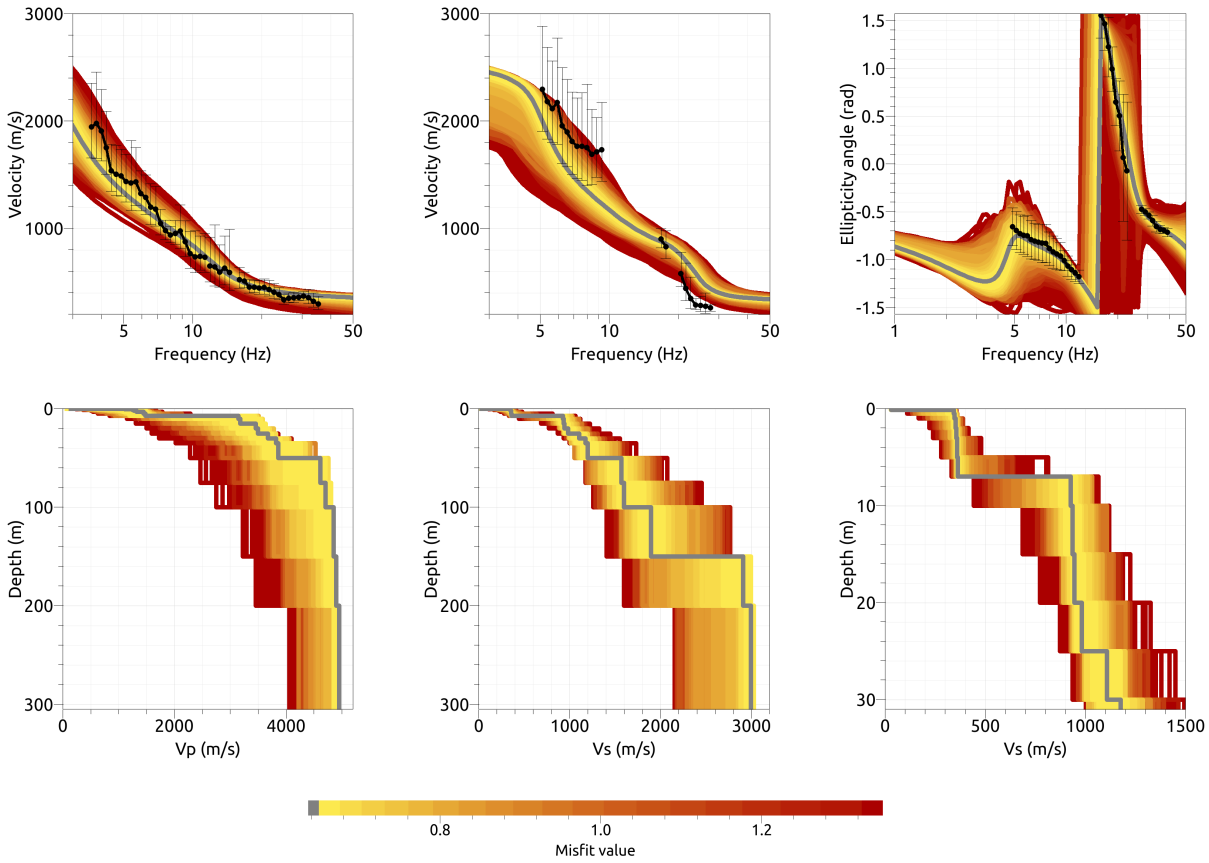

Figure 24: Inversion SWIMfix2. Top line: Dispersion curves for Love waves (left) and Rayleigh waves (center) and Rayleigh wave ellipticity angle (right) of the respective fundamental modes. Bottom line: P-wave velocity profiles (left), S-wave velocity profiles (center and zoom on the upper 30 m on the right). All generated models are plotted on top of each other in the color corresponding to the respective misfit value. The black dots with error bars indicate the data points used for the inversion, the gray line indicates the best-fitting model. In the ellipticity angle plot, the light gray dots and error bars indicate the ellipticity values of targets 2 and 3, which where not used for the inversion here.

4.4 Overview of the inversion result

The best-fitting models of all inversions are shown in Fig. 25. Using target 1, i.e. for the site of the permanent station, we find models with a near-surface shear-wave velocity between 65 and 155 m/s in a first layer of a thickness of about 1 to 1.6 m, followed by velocities between 560 and 650 m/s down to about 10 m, where another velocity increase to about 900 m/s is found. This can therefore be identified as the seismic bedrock. Below, the models show further velocity contrasts between 28 and 36 m to velocities of around 1500 m/s, followed by another gradual velocity increase.
For target 2, i.e. using the small-scale array results centered on the parking lot, a very shallow layer with a thickness of around 0.1 m and a velocity of 30 to 40 m/s is found. This layer is not well constrained by the measured dispersion curves, and would also have a resonance frequency well above the measured frequency range. The models consistently show a second layer with a velocity of about 350 m/s down to about 7.0 m. This layer is responsible for the observed Rayleigh wave ellipticity singularity. At this depth, the velocities increase to values between 920 and 990 m/s, i.e. the seismic bedrock is found at around 7 m here. Another velocity contrast is found below 30 m, followed by another gradual velocity increase.
When comparing the results of both targets, we have to keep in mind that station 42, the reference point for inversion 1, is located 3.7 m higher than station 46, the reference of inversion 2. This is well compatible with the 3 m difference of the seismic bedrock depths resulting from the inversions.
The V_{S30} value for the inversions with target 1 is (673.6 ± 9.9) m/s, and (651.4 ± 2.9) m/s for target 2, where in both cases the 4-layer inversions have been neglected.
In SIA261 and EC8, this corresponds to soil class B for both targets.
As the characterization of the underground at the permanent station SWIM was the main target of the measurement, the inversions using target 1 are taken as representative results for the site.

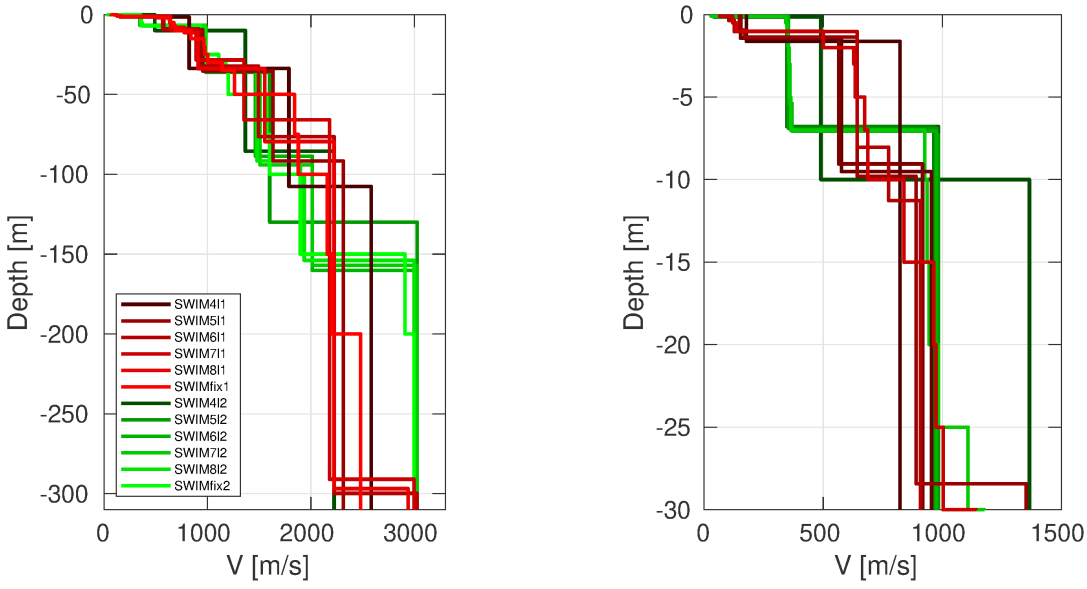

Figure 25: Overview of shear-wave velocity profiles of the best-fitting models of all inversions (left) and a zoom on the shallow part (right).

4.5 Site amplification

In Fig. 26, the theoretical amplification functions for the best models resulting from the different parameterizations for the two targets are compared with the empirical amplification for station SWIM, based on 48 events so far. The empirical amplification of the station is relatively flat and shows a peak at around 6 Hz. The modeled amplification for target 1 is slightly higher, but in good agreement with this empirical amplification, although the modeled peak is below 5 Hz and other peaks are visible which are not present in the empirical amplification. The modeled amplification for target 2 differs more and shows a prominent peak at around 14 Hz, which is not visible in the empirical amplification.

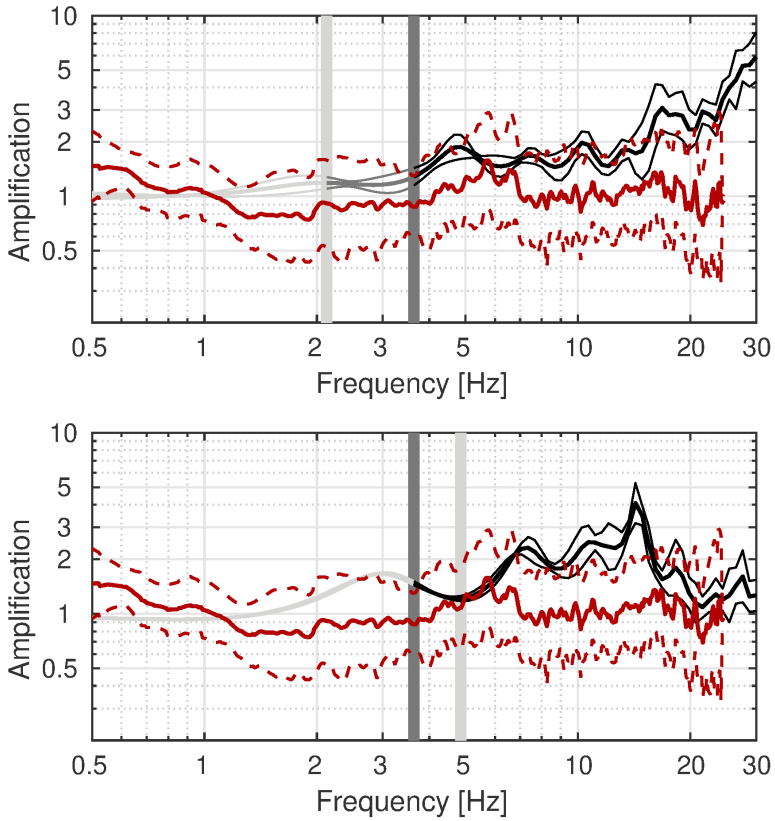

Figure 26: Top: Comparison between the modeled amplification for the best models of the different inversions using target 1 (black curve with standard deviation) and the empirical amplification measured at station SWIM (red, with standard deviation). Bottom: The same for target 2. The vertical light and dark grey bars correspond to the lowest frequency of the ellipticity and dispersion curves, respectively.

4.6 Quarter-wavelength representation

The quarter-wavelength velocity approach (Joyner et al., 1981) provides, for a given frequency, the average velocity at a depth corresponding to 1/4 of the wavelength of interest. It is useful to identify the frequency limits of the experimental data (the minimum frequency of the dispersion curve used in both inversions is 3.62 Hz, the minimum frequency with ellipticity information is about 2.1 Hz for target 1 and 4.87 Hz for target 2). The results using this proxy show that the dispersion curves constrain the profiles down to about 62 m for target 1, and to about 60 m for target 2, and that the ellipticity information extends this range to about 172 m for target 1 (Fig. 27). Moreover, the quarter wavelength impedance-contrast introduced by Poggi et al. (2012) is also displayed in the figure. It corresponds to the ratio between two quarter-wavelength average velocities, respectively from the top and the bottom part of the velocity profile, at a given frequency (Poggi et al., 2012). This curve shows a strong contrast at the fundamental frequency of the site.

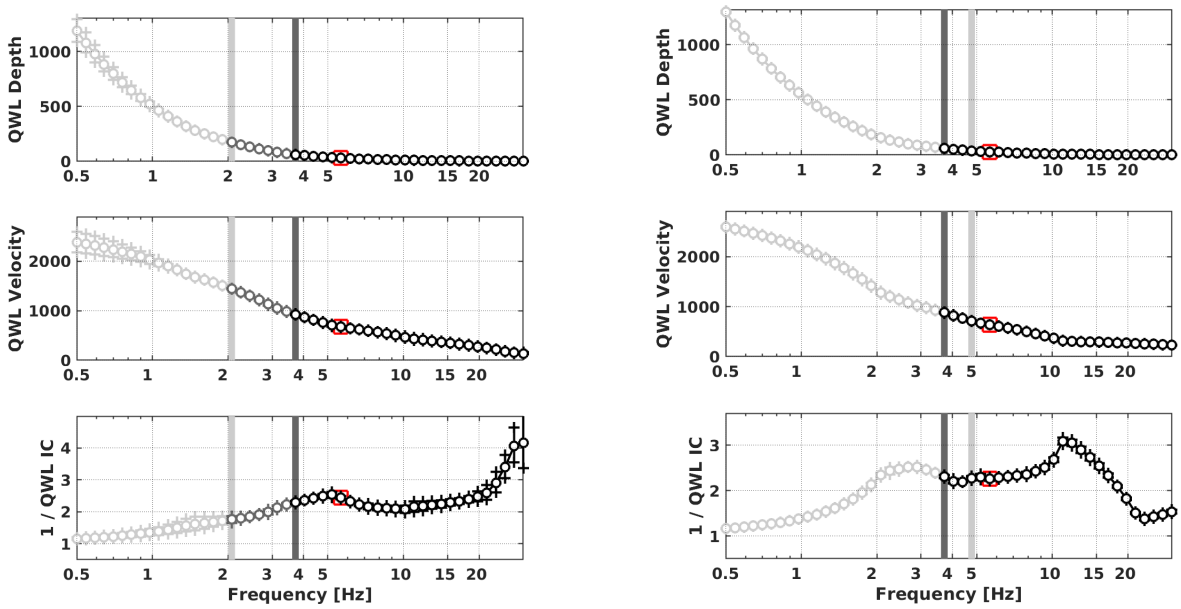

Figure 27: Quarter wavelength representation of the velocity profile for the best models of the inversions (top: depth, center: velocity, bottom: inverse of the impedance contrast). The black curves are constrained by the dispersion curves, the light grey curves are not constrained by the data. The red square corresponds to V_{S30}. The plots show the results for target 1 (left) and target 2 (right).

5 Conclusion

We performed a passive array measurement with two arrays to characterize the soil underneath station SWIM in Wildhaus (SG), located on moraine.
Using the array measurements, we could retrieve dispersion curves for the fundamental mode of Love waves between 3.5 and 37.1 Hz and for the fundamental mode of Rayleigh waves between 4.9 and 28.1 Hz. The high-frequency dispersion curves correspond to the velocities on the parking lot and are not representative for the permanent station SWIM. At this location, the Rayleigh wave ellipticity has peaks at 5.63 and 41.4 Hz, which are both not singularities.
Inversions using two different targets were performed, where the first is representative for station SWIM and the second for the parking lot.
The area around station SWIM is characterized by a shallow layer of 1 to 1.6 m depth and an S-wave velocity between 65 and 155 m/s, followed by a second layer with a velocity between 560 and 650 m/s down to about 10 m, where the seismic bedrock with a velocity of about 900 m/s is found. Below, the velocities gradually increase. The V_{S30} value is (673.6 ± 9.9) m/s. For the second inversion centered on the parking lot, it is (651.4 ± 2.9) m/s.
This corresponds to soil class B for both SIA261 and EC8 in both cases.

Acknowledgements

The authors thank Manuel Studer for his help during the array measurements.

References

Aki, K. (1957). Space and time spectra of stationary stochastic waves, with special reference to microtremors. *Bull. Earthquake Res. Inst. Tokyo Univ.*, 35:415–456.

Bettig, B., Bard, P.-Y., Scherbaum, F., Riepl, J., Cotton, F., Cornou, C., and Hatzfeld, D. (2001). Analysis of dense array noise measurements using the modified spatial auto-correlation method (SPAC): application to the Grenoble area. *Boll. Geof. Teor. Appl.*, 42:281–304.

Burjánek, J., Gassner-Stamm, G., Poggi, V., Moore, J. R., and Fäh, D. (2010). Ambient vibration analysis of an unstable mountain slope. *Geophys. J. Int.*, 180:820–828.

Burjánek, J., Moore, J. R., Molina, F. X. Y., and Fäh, D. (2012). Instrumental evidence of normal mode rock slope vibration. *Geophys. J. Int.*, 188:559–569.

Fäh, D., Wathelet, M., Kristekova, M., Havenith, H., Endrun, B., Stamm, G., Poggi, V., Burjanek, J., and Cornou, C. (2009). Using ellipticity information for site characterisation. NERIES deliverable JRA4 D4, available at http://www.neries-eu.org.

Hobiger, M., Bard, P.-Y., Cornou, C., and Le Bihan, N. (2009). Single station determination of Rayleigh wave ellipticity by using the random decrement technique (RayDec). *Geophys. Res. Lett.*, 36.

Joyner, W. B., Warrick, R. E., and Fumal, T. E. (1981). The effect of Quaternary alluvium on strong ground motion in the Coyote Lake, California, earthquake of 1979. *Bull. Seismol. Soc. Am.*, 71(4):1333–1349.

Maranò, S., Reller, C., Loeliger, H.-A., and Fäh, D. (2012). Seismic waves estimation and wavefield decomposition: Application to ambient vibrations. *Geophys. J. Int.*, 191:175–188.

Poggi, V., Edwards, B., and Fäh, D. (2012). Characterizing the Vertical-to-Horizontal ratio of ground motion at soft-sediment sites. *Bull. Seismol. Soc. Am.*, 102(6):2741–2756.

Poggi, V. and Fäh, D. (2010). Estimating Rayleigh wave particle motion from three-component array analysis of ambient vibrations. *Geophys. J. Int.*, 180:251–267.